Structure of the antidiuretic hormone vasopressin receptor signalling complex.

Julien Bous, Hélène Orcel, Nicolas Floquet, Cedric Leyrat, Josephine Lai-Kee-Him, Gérald Gaibelet, Aurelie Ancelin, Julie Saint-Paul, Stefano Trapani, Maxime Louet, et al.

1   **Structure of the antidiuretic hormone vasopressin receptor signalling complex.**

2

3   Julien Bous[1,2], Hélène Orcel[1], Nicolas Floquet[3,4], Cédric Leyrat[1,4], Joséphine Lai-Kee-Him[2],

4   Gérald Gaibelet[1,5], Aurélie Ancelin[2,6], Julie Saint-Paul[1,7], Stefano Trapani[2], Maxime Louet[3],

5   Rémy Sounier[1], Hélène Déméné[2], Sébastien Granier[1]*, Patrick Bron[2]* & Bernard

6   Mouillac[1]*

7

8   [1]Institut de Génomique Fonctionnelle, Université de Montpellier, CNRS, INSERM, 34094

9   Montpellier cedex 5, France

10   [2]Centre de Biochimie Structurale, Université de Montpellier, CNRS, INSERM, 34090

11   Montpellier, France

12   [3]Institut des Biomolécules Max Mousseron, Université de Montpellier, CNRS, 34093

13   Montpellier cedex 5, France

14   [4]these authors contributed equally

15   [5]present address: AB Science, 13288 Marseille cedex 9, France

16   [6]present address: Laboratoire CiTCoM, CNRS UMR8038, Faculté de Pharmacie,

17   Université Paris Descartes, 75006 Paris, France

18   [7]present address: iMAb, Institut de Recherche en Cancérologie de Montpellier, 34298,

19   Montpellier cedex 5, France

20   *to whom correspondence should be addressed: sebastien.granier@igf.cnrs.fr;

21   patrick.bron@cbs.cnrs.fr; bernard.mouillac@igf.cnrs.fr

22

23   **Arginine-vasopressin (AVP) is a neurohypophysial peptide known as the**

24   **antidiuretic hormone. It forms an active signalling complex with the V2 receptor**

25   **(V2R) and the Gs protein, promoting a cAMP/PKA-dependent aquaporin insertion**

1   **in apical membranes of principal cells of the renal collecting ducts and ultimately,**

2   **water reabsorption. Molecular mechanisms underlying activation of this critical G**

3   **protein-coupled receptor (GPCR) signalling system are still unknown. To fill this**

4   **gap of knowledge, we report here the structure of the AVP-V2R-Gs complex using**

5   **cryo-electron microscopy (cryo-EM). Single-particle analysis revealed the**

6   **presence of three different states. The two best maps were combined with**

7   **computational and NMR spectroscopy constraints to reconstruct two structures of**

8   **the ternary complex. These structures differ in AVP and Gs binding modes and**

9   **could thus represent distinct complex conformations along the signalling**

10   **activation pathway. Importantly, as compared to those of other class A GPCR-Gs**

11   **complexes, the structures revealed an original receptor-Gs interface in which the**

12   **Gsα subunit penetrates deeper into the active V2R, notably forming an ionic bond**

13   **between its free C-terminal carboxylic function and the side chain of R137 in the**

14   **V2R. Interestingly, the structures help to explain how V2R R137H or R137L/C**

15   **variants can lead to two severe genetic diseases with opposite clinical outcomes,**

16   **cNDI or NSIAD respectively. Our study thus provides important structural insights**

17   **into the function of this clinically relevant GPCR signalling complex.**

18

19   The biological actions of AVP, a cyclic nonapeptide, are mediated through three GPCR

20   subtypes, V1a, V1b and V2[1]. In addition, AVP is able to activate the related oxytocin (OT)

21   receptor (OTR)[2]. The V2R is mainly expressed at the basolateral membrane of principal

22   cells of the kidney collecting ducts and governs the crucial physiological function of body

23   water homeostasis[3]. Binding of AVP to the V2R increases cAMP intracellular level via

24   coupling to the adenylyl cyclase stimulatory Gs protein, leading to activation of protein

25   kinase A, phosphorylation of aquaporin 2 water channels[4] and, ultimately to water

1   reabsorption and urine concentration. Activation of the V2R also elicits arrestin-

2   dependent pathways such as receptor internalization and MAP kinase phosphorylation

3   associated with cell growth and proliferation[5,6]. This GPCR is involved in many water

4   balance disorders (hyponatremia consecutive to congestive heart failure, hypertension

5   or hepatic cirrhosis) and voiding disorders (incontinence, nocturia), and as such

6   constitutes a major therapeutic target[7]. Moreover, inactivating and constitutively active

7   mutations in the V2R sequence are responsible for two rare X-linked genetic diseases

8   with opposite clinical outcomes: 1) congenital nephrogenic diabetes insipidus (cNDI)

9   characterized by excessive urine voiding[8], 2) nephrogenic syndrome of inappropriate

10 antidiuresis (NSIAD) characterized by excessive water loading and hyponatremia[9]. V2R

11 is also a target for treating autosomal dominant polycystic kidney disease, the most

12 frequent Mendelian inherited disorder affecting millions of people worldwide[10]. This

13 pathology results from increased cell proliferation, apoptosis and dedifferentiation, in

14 which cAMP- and MAP kinase-dependent signaling pathways are highly activated.

15 The structural biology of GPCRs has made significant progress during the last decade

16 with a wealth of information on ligand binding and G protein coupling that shed light on

17 structural and dynamic aspects of their function[11,12]. Yet V2R like many GPCRs, has been

18 refractory to high-resolution structure determination. Cryo-EM has emerged as a

19 powerful method for the determination of challenging membrane protein structures[13],

20 in particular when the intrinsic structural dynamics of the target prevents the use of

21 crystallogenesis. A growing list of GPCR-G protein complex structures has thus been

22 determined[14,15], revealing key molecular mechanisms of agonist binding and G protein

23 (Gi, Gs, Gq, Go) coupling to class A and class B GPCRs. Here we have developed an *in vitro*

24 purification strategy to reconstitute the GPCR signalling complex comprising the AVP-

25 bound V2R and the heterotrimeric G_s protein stabilized with the nanobody Nb35. Cryo-

3

1   EM single-particle analysis revealed the presence of three distinct populations of the

2   ternary complex with two best maps at a mean resolution of 4.0 and 4.1 Å. A novel

3   hybrid approach was used to build both corresponding structures. Analyses of the

4   structural features of the distinct conformations provide unprecedented molecular

5   insights into the dynamic process of ternary complex formation between the hormone

6   AVP, the V2 receptor and the Gs protein.

7

8   **Determination of the AVP-V2R-Gs-Nb35 complex structure**

9   After extensive biochemical optimization, validation of the complex preparation and of

10   cryo-EM grid sample vitrification, (see Methods, **Extended Data Fig. 1**, **Supplementary**

11   **Figs. 1-2**), a total number of 25,770 movies were recorded, with 3.5 million particles

12   picked and sorted out for further data processing (**Extended data Fig. 2-3**). After 3D

13   classification of projections and 3D refinement, we identified three different

14   conformational states of the complex, referred to as Loose (L), Tight-1 (T1) and Tight-2

15   (T2). Reconstruction of each state was at 4.2 Å, 4.5 Å and 4.7 Å, with a distribution of

16   16%, 48% and 36%, respectively (**Extended Data Fig. 2**), the local resolution varying

17   from 3.2 to 6.4 Å (**Extended data Fig. 3c-d).** Using the recent algorithm developed to

18   enhance cryo-EM maps by density modification[16], the resolution of density maps were

19   improved to 4.0 (L state), 4.1 (T1 state) and 4.5 Å (T2 state), respectively (**Extended**

20   **data Fig. 2, Extended Data Table 1, Supplementary Fig. 3)**. These maps mainly differ

21   in the angle of Gs-Nb35 with the receptor 7TM, and may reflect an inherent high

22   flexibility of the complex. A conformational heterogeneity analysis using multi-body

23   refinement revealed that more than 78% of the variance is accounted for by the fourth

24   first eigenvectors related to rotations and translations between AVP-V2R and Gs-Nb35

25   (**Extended Data Fig. 4**, **Extended data Movie 1**). The 4.5 Å map of the T2 state was not

1 well enough resolved to compute a reliable structure. Therefore, only the L and T1

2 structures, referred to as L and T states, were used for further analysis.

3 Because we could not unambiguously build the AVP in the calculated maps, we designed

4 an original hybrid strategy based on a combination of cryo-EM maps, computational

5 molecular dynamic simulations and experimental saturation transfer difference (STD)

6 NMR (**Fig. 1a-e**, **Supplementary Discussion and Figs. 4-8**). Based on this approach, the

7 L and T models were then built in a more conventional manner to match as closely as

8 possible the density maps (**Fig. 1f-g, Extended Data Table 1**).

9 In the final models, side chains of most residues are clearly identifiable in the 7 TM and

10 helix 8 of the V2R in both structures (**Extended Data Fig. 5**). Intracellular loop1 (ICL1)

11 was well defined in the maps, as well as the contacts between V2R and the Gs protein.

12 The α–helical domain of Gαs subunit was subtracted during single particle analysis for

13 high-resolution map refinement. Intracellular loops 2 and 3 and the C-terminus of V2R

14 were not seen in the density maps, and were not constructed in the final models.

15

16 **Overall architecture of the ternary complex**

17 Both L and T AVP-V2-Gs ternary complexes present a typical GPCR-G protein

18 architecture with the receptor 7TM helix bundle engaging the peptide agonist on the

19 extracellular side and the Gαs C-terminus domain (α5 helix) on the intracellular side

20 (**Fig 2a-d**). However, the L and T states present large structural differences most

21 notably in the position of the G protein heterotrimer relative to V2R (**Fig. 2e**). The α5

22 helix interacts more tightly in the T state than in the L state (**Fig. 2b and 2d**), inducing a

23 translation of the whole Gs heterotrimer (**Fig. 2e**). In particular, the α4 helix and the

24 Ras-like domain of Gαs are translated from 4 Å and 5 Å between the L and T states,

25 respectively. These movements position the αN helix 5 Å closer to the receptor in the T

1   state in comparison to the L state (**Fig. 2e**). Those Gα movements are also accompanied

2   by a 7 Å translation of the Gβ N-terminal helix, a translation of the γ subunit of 6 Å and a

3   translation of Nb35 of 7 Å (**Fig. 2e**).

4   The presence of several conformational states and the multi-body refinement analysis

5   reflect the dynamics of V2-Gs complex formation. From the final L structure model, a

6   principal component analysis (PCA) obtained from classical molecular dynamic

7   simulations revealed similar dynamics and suggests that the conformations captured by

8   the cryo-EM 3D reconstructions represent averaged states that are part of a much larger

9   conformational ensemble (**Extended data Movie 2, Supplementary Fig. 9**). Though

10 those differences are less pronounced that the ones recently described for the

11 neurotensin receptor NTSR1-Gi1 complexes[17], they further indicate that GPCR-G protein

12 coupling is a dynamic process in which the G protein may explore different set of

13 conformations.

14

15 **AVP binding pocket within V2R and comparison with OTR binding site**

16 Our hybrid approach allowed us to build convincing models of AVP binding poses in

17 both L and T structures. The final calculated structures present a central position of AVP

18 in the orthosteric pocket of the V2R along the axis of the helical bundle **(Fig. 3,**

19 **Extended Data Fig. 6)**. The extracellular domains of the V2R are widely opened in both

20 L and T conformations, a feature consistent with the accommodation of a cyclic peptide

21 like AVP (**Extended Data Fig. 6**), and in agreement with the recently reported inactive

22 OTR structure[18]. In the L and T structures, AVP contacts residues from both TM helices

23 and extracellular loops **(Fig. 3a-c, Extended Data Fig. 6)** in agreement with what was

24 originally proposed based on pharmacological data[19]. Consistent with its amphipathic

1   nature, AVP interacts with two chemically distinct interfaces in a 15 Å deep binding

2   pocket to form both polar and hydrophobic contacts **(Fig. 3a- c)**.

3   While AVP conformations occupy a central position in both the L and T binding clefts,

4   interesting changes are observed due to a translation of the Tyr^2 residue side-chain

5   (from TM7 to TM3), and to a movement of the C-terminal tripeptide (inversion in Arg^8

6   and Gly^9-NH_2 positions) at the V2R surface (**Extended data Fig. 6**). The cyclic part of

7   AVP (Cys^1 to Cys^6) and the Pro^7 are buried into the cleft defined by the seven-helix

8   bundle of V2R, leaving only Arg^8 residue and C-terminal glycinamide exposed to the

9   solvent (**Extended data Fig. 6).** In both the L and T structures, the Cys^1-Tyr^2-Phe^3

10   hydrophobic motif of AVP binds deeper in the binding site creating key contacts with the

11   receptor (**Fig. 3a-c**), in agreement with STD spectroscopy data (**Fig. 1**).

12   V2R and OTR belong to the same subfamily of peptide class A GPCRs and share a

13   common orthosteric binding site[19,20]. Although V2R and OTR (PDB 6TPK) structures[18]

14   represent different GPCR conformations (active agonist-bound V2R *vs* inactive

15   antagonist-bound OTR), it is interesting to compare the complete set of residues

16   involved in the binding of the natural hormone AVP with the ones involved in retosiban

17   binding to gain insights into ligand binding and efficacy in this receptor family **(Fig 3b-**

18   **e).** Many OTR residues involved in the binding of retosiban are actually conserved

19   among AVP/OT receptors and also interact with AVP in the V2R **(Fig. 3b-e).**

20   Interestingly, the conserved $W^{6.48}$ and $F^{6.51}$ (Ballesteros-Weinstein numbering) in

21   AVP/OT receptors, interact with the highly hydrophobic indanyl moiety of retosiban in

22   the crystal structure of inactive OTR. AVP also makes contact with $F^{6.51}$ through its Tyr^2

23   but is not in contact with $W^{6.48}$ in the V2R, probably because it is too bulky to bind

24   deeper in the pocket. These data confirm that hydrophobic small molecule nonpeptide

1 antagonists and AVP partially superimpose at the bottom of the orthosteric binding

2 pocket of AVP/OT receptors **(Fig. 3d-e)**[21,22,23].

3

4 **Activation of the V2R and comparison with other class A GPCRs**

5 The active-state structures of the V2R reveal key structural features of the activation

6 process by comparison with the OTR inactive structure (**Fig. 4a-e**). Moreover, to get a

7 more general view of V2R activation, it was also important to look at the canonical

8 conformational changes of TMs and of conserved motifs involved in other ligand-

9 activated GPCRs of class A[24,25]. Thus, compared to other active GPCR structures and to

10 the inactive antagonist-bound OTR structure (**Fig. 4, Supplementary Fig. 10**), the L and

11 T structures of V2R present all the features of active conformations, i.e. a large-scale

12 displacement of TM6 (**Fig. 4a**), conformational changes of $W^{6.48}$ toggle switch **(Fig. 4b)**,

13 a rearrangement of the $P^{5.50}$-$S^{3.40}$-$Y^{6.44}$ transmission switch, equivalent to the PIF motif in

14 other GPCRs (**Fig. 4c**), a rotation of the conserved $NPxxY^{7.53}$ motif **(Fig. 4d)** and a broken

15 $D136^{3.49}$-$R137^{3.50}$ ionic lock (**Fig 4e, Fig. 5e**).

16 Importantly by comparing the structures of the inactive antagonist-bound OTR with the

17 active agonist-bound V2R, it appears that contacts between $M123^{3.36}$ and $F287^{6.51}$-

18 $W284^{6.48}$ motif (all in contact with Tyr^{2} of AVP) undergo large conformational

19 rearrangements (**Extended Data Fig. 6**). It is thus tempting to speculate that it is a key

20 motif regulating the activity of this family of receptor.

21 As indicated above, the V2R $R137^{3.50}$ participates in the ionic lock motif involved in the

22 balance of active *versus* inactive states of class A GPCRs[24]. In the inactive structure of

23 OTR (**Fig. 4e**), $D136^{3.49}$ and $R137^{3.50}$ interact with each other through this ionic lock. For

24 comparison, this salt bridge is broken in the L and T active conformations of the V2R-Gs

25 complex (**Fig. 4e, Fig. 5e**). The observed constitutive activity towards Gs coupling for

1   the missense mutations C137[3.50] or L137[3.50] responsible for NSIAD[9,26,27] can thus be

2   explained from a structural point of view since these hydrophobic residues are not able

3   to form such an ionic lock to stabilize the inactive state. On the contrary, the mutant

4   H137[3.50] causing cNDI[28,29] might still be able to maintain the balance between active and

5   inactive states of the V2R through its partial positive charge. Its loss-of-function rather

6   reflects the loss of accessibility to AVP because of a constitutive internalization[27, ,28,29].

7

8   **V2R-Gs interactions**

9   The cryo-EM maps of the ternary complex clearly establish the structural details of V2R-

10   Gs coupling. As anticipated from the conserved mechanism of GPCR-G protein

11   coupling[30,31], both the L and T conformations show a similar overall architecture of the

12   complex interface with the engagement of the Gαs C-terminal α5 helix in the core of the

13   7TM **(Fig. 5, Extended Data Fig. 7, Supplementary Fig. 10)**. However, there are some

14   interesting differences compared to other GPCR-Gs complex structures. Of note, in both

15   the L and T structures, the V2R ILC1 makes many direct contacts with the Gβ subunit. In

16   the T state, ICL1 residues L62-A63-R64-R65-G66 interact with Gβ R52, D312-N313 and

17   D333-F335 (**Fig5a**). In the L state, ICL1 residues R65-G66-R67-R68 interact with Gβ

18   R52, D312 and D333 (**Extended Data Fig. 7a**). These contacts between V2R and Gβ are

19   much more numerous than in the class A GPCR β2AR- or A$_{2A}$R-Gs complexes[32,33].

20   Moreover in the T conformation, there are some additional contacts between V2R ICL1

21   (R67-G69-H70) with the N-terminal α helix of Gαs (Q31, Q35 and R38), resulting in a

22   more compact interaction (**Fig 5b**). In the L state, V2R (W71) and N-terminal α helix of

23   Gαs (Q35 and R38) contacts are more limited (**Extended Data Fig. 7b**). Contacts

24   between the N-terminal α helix of Gαs with GPCRs have only been seen in GLP1R and

25   CTR class B GPCR complexes[34,35], not in class A GPCR-G complexes.

1   In contrast to what was observed for the β2AR[32] and the μOR[36], the Gαs C-terminal α5

2   helix appears to extend helix 8 (H8) of the V2 receptor, lying almost parallel to the

3   membrane plane **(Fig. 5c, Extended Data Fig 7c, f-h)**. Also, compared with the β2AR,

4   the C-terminus of Gαs is interacting deeper in the V2R 7TM core making direct contact

5   with residues (L and T states, respectively) of V2R that are part or in close proximity to

6   the conserved NPxxY (TM7) and DRH (TM3) activation motifs **(Fig 5d-e, Extended Data**

7   **Fig. 7d-h)**. In this respect, the V2-Gs interaction resembles more the interaction seen in

8   the μOR-Gi complex **(Extended Data Fig. 7f-h)**. The V2R TM7-H8 hinge region also

9   makes a strong contact with the Gαs ELL motif, in particular through hydrophobic

10   contacts with the F328$^{7.56}$ side chain **(Fig. 5d)**. The T and L conformations differ here in

11   the position of the Gαs L394 side chain originating from a distinct F328$^{7.56}$ side chain

12   conformation (pointing towards I78$^{2.43}$ of the receptor in the T structure or towards Gαs

13   L394 in the L structure) (**Fig. 5d, Extended Data Fig. 7d**). Most notably in the T state,

14   the side chain of R137$^{3.50}$ which is part of the ionic lock motif, forms an ionic interaction

15   with the free carboxylic acid function of the Gαs C-terminus (**Fig. 5e**), a direct contact

16   that was not observed before between a GPCR and a G protein of any family (Gs, Gi, Go

17   or Gq)[14,15,37]. Moreover, in the L state, the density map suggests that the R137$^{3.50}$ side

18   chain could adopt two conformations, one forming a similar ionic interaction with the

19   carboxylic acid of Gαs L394 main chain, and, the other one, pointing towards the

20   Y325$^{7.53}$ from the NPxxY motif (**Extended Data Fig. 7e).**

21

22   **Conclusion**

23   In this study, we solved two structures of the active state of the AVP hormone-bound

24   V2R in complex with the Gs protein. The structural insights into the function of this

1   signalling system pave the way for future drug development to treat water balance

2   disorders[7].

3

4   **References**

5

6   1.   Barberis, C., Mouillac, B. & Durroux, T. Structural bases of vasopressin/oxytocin

7   receptor function. *J. Endocrinol.* **156**, 223–9 (1998).

8   2.   Barberis C., Morin D., Durroux T., Mouillac B., Guillon G., Seyer R., Hibert M, T. E.

9   and M. M. Molecular Pharmacology of AVP and OT Receptors and Therapeutic

10   Potential. *Drug News Perspect.* **12**, 279–292 (1999).

11   3.   Robben, J. H., Knoers, N. V. A. M. & Deen, P. M. T. Regulation of the vasopressin V2

12   receptor by vasopressin in polarized renal collecting duct cells. *Mol. Biol. Cell* **15**,

13   5693–9 (2004).

14   4.   Treschan, T. A. & Peters, J. The vasopressin system: physiology and clinical

15   strategies. *Anesthesiology* **105**, 599–612; quiz 639–40 (2006).

16   5.   Ren, X. R. *et al.* Different G protein-coupled receptor kinases govern G protein and

17   β-arrestin-mediated signaling of V2 vasopressin receptor. *Proc. Natl. Acad. Sci. U.*

18   *S. A.* **102**, 1448–1453 (2005).

19   6.   Alonso, G. *et al.* Sustained elevated levels of circulating vasopressin selectively

20   stimulate the proliferation of kidney tubular cells via the activation of V2

21   receptors. *Endocrinology* **150**, 239–50 (2009).

22   7.   Ball, S. G. Vasopressin and disorders of water balance: the physiology and

23   pathophysiology of vasopressin. *Ann. Clin. Biochem.* **44**, 417–31 (2007).

24   8.   Morello, J. P. & Bichet, D. G. Nephrogenic diabetes insipidus. *Annu. Rev. Physiol.* **63**,

25   607–30 (2001).

1 9.   Feldman, B. J. *et al.* Nephrogenic syndrome of inappropriate antidiuresis. *N. Engl. J.*

2   *Med.* **352**, 1884–90 (2005).

3 10. Harris, P. C. & Torres, V. E. Polycystic kidney disease. *Annu. Rev. Med.* **60**, 321–37

4   (2009).

5 11. Edward Zhou, X., Melcher, K. & Eric Xu, H. Structural biology of G protein-coupled

6   receptor signaling complexes. *Protein Sci.* **28**, 487–501 (2019).

7 12. Gusach, A. *et al.* Beyond structure: emerging approaches to study GPCR dynamics.

8   *Curr. Opin. Struct. Biol.* **63**, 18–25 (2020).

9 13. Fernandez-Leiro, R. & Scheres, S. H. W. Unravelling biological macromolecules

10   with cryo-electron microscopy. *Nature* **537**, 339–46 (2016).

11 14. Carpenter, B. & Tate, C. G. Active state structures of G protein-coupled receptors

12   highlight the similarities and differences in the G protein and arrestin coupling

13   interfaces. *Curr. Opin. Struct. Biol.* **45**, 124–132 (2017).

14 15. García-Nafría, J. & Tate, C. G. Cryo-EM structures of GPCRs coupled to G s , G i and

15   G o. *Molecular and Cellular Endocrinology* vol. 488 1–13 (2019).

16 16. Terwilliger, T. C., Ludtke, S. J., Read, R. J., Adams, P. D. & Afonine, P. V.

17   Improvement of cryo-EM maps by density modification. *Nat. Methods* **17**, 923–

18   927 (2020).

19 17. Kato, H. E. *et al.* Conformational transitions of a neurotensin receptor 1–Gi1

20   complex. *Nature* **572**, 80–85 (2019).

21 18. Waltenspühl, Y., Schöppe, J., Ehrenmann, J., Kummer, L. & Plückthun, A. Crystal

22   structure of the human oxytocin receptor. *bioRxiv* 2020.02.21.958090 (2020)

23   doi:10.1101/2020.02.21.958090.

24 19. Mouillac, B. *et al.* The binding site of neuropeptide vasopressin V1a receptor.

25   Evidence for a major localization within transmembrane regions. *J. Biol. Chem.*

270, 25771–7 (1995).

20. Hibert, M. *et al.* Functional architecture of vasopressin/oxytocin receptors. *J. Recept. Signal Transduct. Res.* **19**, 589–96 (1999).

21. Macion-Dazard, R. *et al.* Mapping the Binding Site of Six Nonpeptide Antagonists to the Human V 2 -Renal Vasopressin Receptor. *J. Pharmacol. Exp. Ther.* **316**, 564–571 (2006).

22. Cotte, N. *et al.* Conserved aromatic residues in the transmembrane region VI of the V 1a vasopressin receptor differentiate agonist vs. antagonist ligand binding. *Eur. J. Biochem.* **267**, 4253–4263 (2000).

23. Tahtaoui, C. *et al.* Identification of the Binding Sites of the SR49059 Nonpeptide Antagonist into the V 1a Vasopressin Receptor Using Sulfhydryl-reactive Ligands and Cysteine Mutants as Chemical Sensors. *J. Biol. Chem.* **278**, 40010–40019 (2003).

24. Filipek, S. Molecular switches in GPCRs. *Curr. Opin. Struct. Biol.* **55**, 114–120 (2019).

25. Deupi, X. Relevance of rhodopsin studies for GPCR activation. *Biochim. Biophys. Acta - Bioenerg.* **1837**, 674–682 (2014).

26. Tenenbaum, J. *et al.* The constitutively active V2 receptor mutants conferring NSIAD are weakly sensitive to agonist and antagonist regulation. *PLoS One* **4**, 1–6 (2009).

27. Rochdi, M. D. *et al.* Functional characterization of vasopressin type 2 receptor substitutions (R137H/C/L) leading to nephrogenic diabetes insipidus and nephrogenic syndrome of inappropriate antidiuresis: implications for treatments. *Mol. Pharmacol.* **77**, 836–45 (2010).

28. Bernier, V. *et al.* Functional rescue of the constitutively internalized V2

1   vasopressin receptor mutant R137H by the pharmacological chaperone action of

2   SR49059. *Mol. Endocrinol.* **18**, 2074–84 (2004).

3   29. Barak, L. S., Oakley, R. H., Laporte, S. A. & Caron, M. G. Constitutive arrestin-

4   mediated desensitization of a human vasopressin receptor mutant associated with

5   nephrogenic diabetes insipidus. *Proc. Natl. Acad. Sci. U. S. A.* **98**, 93–8 (2001).

6   30. Weis, W. I. & Kobilka, B. K. The Molecular Basis of G Protein-Coupled Receptor

7   Activation. *Annu. Rev. Biochem.* **87**, 897–919 (2018).

8   31. Hilger, D., Masureel, M. & Kobilka, B. K. Structure and dynamics of GPCR signaling

9   complexes. *Nat. Struct. Mol. Biol.* **25**, 4–12 (2018).

10 32. Rasmussen, S. G. F. *et al.* Crystal structure of the β2 adrenergic receptor-Gs protein

11   complex. *Nature* **477**, 549–55 (2011).

12 33. García-Nafría, J., Lee, Y., Bai, X., Carpenter, B. & Tate, C. G. Cryo-EM structure of the

13   adenosine A2A receptor coupled to an engineered heterotrimeric G protein. *Elife*

14   **7**, (2018).

15 34. Liang, Y.-L. *et al.* Cryo-EM structure of the active, Gs-protein complexed, human

16   CGRP receptor. *Nature* **561**, 492–497 (2018).

17 35. Liang, Y. L. *et al.* Phase-plate cryo-EM structure of a class B GPCR-G-protein

18   complex. *Nature* **546**, 118–123 (2017).

19 36. Koehl, A. *et al.* Structure of the μ-opioid receptor–Gi protein complex. *Nature* **558**,

20   547–552 (2018).

21 37. Kim, K. *et al.* Structure of a Hallucinogen-Activated Gq-Coupled 5-HT2A Serotonin

22   Receptor. *Cell* **182**, 1574-1588.e19 (2020).

23

1   **METHODS**

2

3   **Data analysis and Figure preparation**

4   Figures were created using the PyMOL 2.3.5 Molecular Graphics System (Schrödinger,

5   LLC) and the UCSF Chimera X 0.9 package. Data were plotted with GraphPad Prism 8.3.0.

6

7   **V2R expression and purification**

8   The version of the human V2R used for this study in described in Supplementary

9   Methods and was cloned into a pFastBac™1 vector. It was expressed in Sf9 insect cells

10   using the Bac-to-Bac® baculovirus expression system ((Thermofisher) according to

11   manufacturer's instructions. Insect cells were grown in suspension in EX-CELL® 420

12   medium (SigmaAldrich) to a density of 4×10^6 cells per ml and infected with the

13   recombinant baculovirus at a MOI of 2-3. The culture medium was supplemented with

14   the V2R pharmacochaperone antagonist Tolvaptan (TVP, SigmaAldrich) at 1 µM to

15   increase the receptor expression levels[38,39]. The cells were infected for 48h-54h at 28°C

16   and expression of the V2R was checked by immunofluorescence using an anti-Flag M1

17   antibody coupled to Alexa488. Cells were then harvested by centrifugation (2 steps, 20

18   min, 3,000xg) and pellets were stored at −80°C until use.

19   The cell pellets were thawed and lysed by osmotic shock in 10 mM Tris-HCl pH 8, 1 mM

20   EDTA buffer containing 2mg.ml⁻¹ iodoacetamide, Tolvaptan 1 µM and protease

21   inhibitors (leupeptine 5µg.ml⁻¹, benzamidine 10µg.ml⁻¹ and PMSF 10µg.ml⁻¹). After

22   centrifugation   (15 min, 38,400xg), the pellet containing crude membranes was

23   solubilized using a glass dounce tissue grinder (15 + 20 strokes using A and B pestles,

24   respectively) in a solubilization buffer containing 20 mM Tris-HCl pH 8, 500 mM NaCl,

25   0.5 % (w/v) n-dodecyl-β-D-maltopyranoside (DDM, Anatrace), 0.2% (w/v) sodium

15

1   cholate (SigmaAldrich), 0.03 % (w/v) cholesteryl hemisuccinate (CHS, SigmaAldrich), 20

2   % Glycerol, 2 mg.ml^{-1} iodoacetamide, 0.75 ml.L^{-1} Biotin Biolock (IBA), Tolvaptan 1 μM

3   and protease inhibitors. The extraction mixture was stirred for 1 h at 4 °C and

4   centrifuged (20 min, 38,400xg). The cleared supernatant was poured onto an

5   equilibrated Strep-Tactin® resin (IBA) for a first affinity purification step. After 2h of

6   incubation at 4°C under stirring, the resin was washed three times with 10 CV of a buffer

7   containing 20 mM Tris-HCl pH 8, 500 mM NaCl, 0.1 % (w/v) DDM, 0.02% (w/v) sodium

8   cholate, 0.03 % (w/v) CHS, Tolvaptan 1 μM. The bound receptor was eluted in the same

9   buffer supplemented with 2.5 mM desthiobiotin (IBA).

10   The eluate was supplemented with 2mM $CaCl_2$ and loaded onto a M1 anti-Flag affinity

11   resin (SigmaAldrich). The resin was washed with 10 CV of two successive buffers

12   containing 20 mM HEPES pH 7.5, 100 mM NaCl, 0,1% DDM, 0,01% CHS, 10 μM AVP,

13   2mM $CaCl_2$, then 20 mM HEPES pH 7.5, 100 mM NaCl, 0,025% DDM, 0,005% CHS, 10 μM

14   AVP, 2mM $CaCl_2$, respectively. The receptor was eluted from the Flag resin using a buffer

15   containing 20 mM HEPES pH 7.5, 100 mM NaCl, 0,025% DDM, 0,005% CHS, 10 μM AVP,

16   2 mM EDTA and 200 μg/mL Flag peptide (Covalab).

17   After concentration using a 50kDa MWCO concentrator (Millipore), the V2R was purified

18   by size exclusion chromatography (SEC) using a Superdex 200 (10/300 column)

19   connected to an AKTA purifier system (GE Healthcare). Fractions corresponding to the

20   pure monomeric receptor were pooled (∼ 2 ml) and concentrated to 50-100 μM with an

21   excess of AVP (200 μM).

22

23   **Gs expression and purification**

24   Human Gαs, Gβ1 with a N-terminal Twin-Strep-tag® and Gγ2 were all expressed in Sf9

25   insect cells grown in EX-CELL® 420 medium (SigmaAldrich). A recombinant

16

1   baculovirus for Gαs subunit was prepared using the BestBac™ (Expression Systems)

2   strategy, whereas a baculovirus for Gβ1 and Gγ2 was prepared using the Bac-to-Bac®

3   system. Gβ1 and Gγ2 were cloned in tandem into the pFastBac™ Dual vector

4   (Thermofisher). Sf9 cells, at a density of $4x10^6$ cells/ml, were co-infected with both

5   viruses at a 1:2 Gαs:Gβ1γ2 ratio for 72h at 28°C. Cells were harvested and pellets stored

6   at -80°C.

7   Co-infected Sf9 cell pellets were thawed and lysed in a buffer containing 10 mM TRIS pH

8   7.4, 1mM EDTA, 5 mM β-Mercapto-Ethanol, 10 μM GDP and protease inhibitors

9   (leupeptine $5\mu g.ml^{-1}$, benzamidine $10\mu g.ml^{-1}$ and PMSF $10\mu g.ml^{-1}$). Lysed cells were

10   centrifuged (20 minutes, 38,400xg). The pellets containing the crude membranes were

11   homogeneized using a glass dounce tissue grinder (20 strokes with tight B pestle) in

12   solubilization buffer containing 20 mM HEPES pH 7.5, 100 mM NaCl, 1% DDM, 5 mM

13    $MgCl_2$ supplemented with 5 mM β-Mercapto-Ethanol, 10 μM GDP, 0.75 $ml.L^{-1}$ biotin

14   biolock and protease inhibitors. The mixture was stirred for 40 minutes at 4°C and

15   centrifuged (20 min, 38,400xg). The supernatant was loaded onto a Strep-Tactin®

16   affinity resin equilibrated with the same buffer. The resin was washed 3 times, first with

17   5 CV of solubilization buffer, then with 5 CV of solubilisation buffer supplemented with

18   100 μM TCEP (instead of β-Mercapto-Ethanol), and finally with 10 CV of wash buffer

19   containing 20 mM HEPES pH 7.5, 50 mM NaCl, 0.1% DDM, 1 mM $MgCl_2$, 100 μM TCEP, 10

20   μM GDP. The Gs heterotrimer protein was eluted in the same buffer supplemented with

21   2.5 mM desthiobiotin. After a treatment with antarctic phosphatase (5 Units, NEB Inc.)

22   for 30 minutes at 4°C, the Gs protein was concentrated to 10 mg/ml using 50 kDa MWCO

23   concentrators. 20% glycerol was added to the sample and aliquots were flash-frozen in

24   liquid nitrogen before storage at -80 °C.

25

1 **Nb35 expression and purification**

2 The production and purification of Nb35 were performed following a protocol

3 established by Kobilka and coworkers[40]. It is described in Supplementary Methods.

4

5 **Purification of the AVP-V2R-Gs-Nb35 complex**

6 Formation of a stable complex was done by mixing the purified V2R with 1.2 molar

7 excess of purified Gs heterotrimer, 250 µM AVP and 2.5 mM $MgCl_2$. The coupling

8 reaction was allowed to proceed at RT for 45 minutes and was followed by addition of

9 apyrase (0.0125 Units, NEB Inc.) to hydrolyse residual GDP and maintain the high-

10 affinity nucleotide-free state of Gs. 15 minutes later, Nb35 was added at a 2-fold molar

11 excess compared to Gs. After 15 more minutes at RT, the mix was incubated overnight at

12 4°C. In most reaction mixtures, the final concentration of V2R was 20-30 µM, that of Gs

13 30-40 µM and the one of Nb35 around 80 µM. To remove excess of G protein

14 heterotrimer and Nb35, the complex AVP-V2R-Gs-Nb35 was purified by a M1 anti-Flag

15 affinity chromatography. After loading, the DDM detergent was then gradually

16 exchanged with Lauryl Maltose Neopentyl Glycol (LMNG, Anatrace). The LMNG

17 concentration was then decreased gradually from 0.5% to 0.01%. The complex and the

18 unbound V2R were eluted in 20 mM HEPES pH 7.5, 100 mM NaCl, 0.01% LMNG, 0.002%

19 CHS, 2 mM EDTA, 10 µM AVP and 0.2 mg.mL^{-1} Flag peptide. The eluted AVP-V2R-Gs-

20 Nb35 complex was separated from unbound V2R by SEC on a Superdex 200 10/300

21 with a buffer containing 20 mM HEPES pH 7.5, 100 mM NaCl, 0.002% LMNG, 0.0025%

22 glyco-diosgenin (GDN, Anatrace), 0.002% CHS, 10 µM AVP. The fractions corresponding

23 to the complex were collected, concentrated with a 50 kDa MWCO concentrator and

24 subjected to a second SEC on a Superose 6 (10/300 GL, GE Healthcare) with a buffer

25 containing 20 mM HEPES pH 7.5, 100 mM NaCl, 0.0011% LMNG, 0.001% GDN, 0.002%

1   CHS, 10 μM AVP. Peak fractions were pooled and concentrated using a 50 kDa MWCO

2   concentrator to concentrations ranging from ~1 mg.mL^{-1} to ~4 mg.mL^{-1} for Cryo-EM

3   studies. The amphipol A8-35 (Anatrace) was added at 0.001% to help in the dispersion

4   of the particles for Cryo-EM grid preparation.

5

6   **Negative stain microscopy observations**

7   Before preparing Cryo-EM grids, we first checked the quality and the homogeneity of the

8   AVP-V2R-Gs-Nb35 sample by NS-EM. The procedure is described in Supplementary

9   Methods.

10

11   **Cryo-EM sample preparation, image acquisition**

12   In this study, two datasets have been recorded from two different preparations of AVP-

13   V2R-Gs-Nb35. For the first dataset acquisition, 3 μL of purified AVP-V2R-Gs-Nb35 at

14   0.75 mg/ml concentration were applied on glow-discharged Quantifoil R 1.2/1.3 300

15   mesh copper holey-carbon grids (Quantifoil Micro tools GmbH, Germany), blotted for

16   4.5s and then flash-frozen in liquid ethane using the semi-automated plunge freezing

17   device Vitrobot Mark IV (ThermoFisher) maintained at 100% relative humidity and 4°C.

18   For the second dataset acquisition, cryo-EM grids were prepared as previously, but the

19   purified V2R-Gs-Nb35 complex was at a concentration of 4 mg/ml and the cryo-EM grids

20   were prepared using a EM GP2 (Leica microsystems) plunge freezer with a 4s blotting

21   time (100% humidity and 4°C).

22   Images were collected in 2 independent sessions on a TEI Titan Krios (ThermoFisher) at

23   the EMBL of Heidelberg (Germany) at 300 keV through a Gatan Quantum 967 LS energy

24   filter using a 20 eV slit width in zero-loss mode and equipped with a K2-Summit (Gatan

25   inc.) direct electron detector configured in counting mode. Movies were recorded at a

1   nominal EFTEM (energy-filtered transmission electron microscope) magnification of

2   ×165,000 corresponding to 0.81 Å calibrated pixel size. The movies were collected in 40

3   frames in defocus range between −0.8 and −2.2 μm with a total dose of 50.19 $e^-/Å^2$ (1st

4   dataset) and 41.19 $e^-/Å^2$ (2nd dataset). Data collection was fully automated using

5   SerialEM[41].

6

7   **Cryo-EM data processing**

8   All data processing operations were performed with RELION-3.0.7[42] unless otherwise

9   specified.

10   In total, 17,290 movies of the AVP-V2R-Gs-Nb35 sample at 0.75 mg/ml were collected.

11   Dose-fractionated image stacks were subjected to beam-induced motion correction and

12   dose-weighting using Motioncorr own implementation. Gctf was used to determine the

13   contrast transfer function parameters[43] from non-dose weighted images. After sorting,

14   micrographs with maximum estimated resolution beyond 5 Å were discarded. Particle

15   picking was carried out using Gautomatch (K. Zhang, MRC LMB (www.mrc-

16   lmb.cam.ac.uk/kzhang/)) allowing to pick out 2,291,432 particles. Particles were

17   extracted in a box-size of 240 Å, downscaled to 4 Å/pix and subjected to reference-free

18   2D classifications to discard false-positive particles or particles categorized in poorly

19   defined classes. A subset of 1,109,475 particles was selected for further processing. This

20   particle set was subjected to a 3D classification with four classes using the 30 Å low-pass

21   filtered calcitonin receptor map as reference[35]. Particles from the 2 classes representing

22   27% of total particles and showing a complete AVP-V2R-Gs-Nb35 complex were

23   selected, re-extracted with a pixel size of 1.62 Å, and subjected to a 3D refinement. This

24   subset of 307,125 particles yielded a map with a global resolution (FSC = 0.143) of 4.8 Å

25   resolution. Particles were then subjected to a focused 3D classification without angular

1   and translational alignments with a mask including the complex minus GαsAH. The best

2   class corresponding to 150,000 particles were re-extracted without binning and

3   submitted to a 3D refinement, allowing us to obtain a map at 4.4 Å resolution. All further

4   processing including signal substraction, using of different type of masks, CTF

5   refinement and polishing did not improved the resolution of the map.

6   In total, 8,490 movies of the AVP-V2R-Gs-Nb35 sample at 4.0 mg/ml were recorded. The

7   image processing steps were the same as previously described, except that the picking

8   was performed using boxnet from Warp software package[44] allowing us to extract

9   1,214,575 particles. After a 2D classification to clean the dataset, a subset of 917,990

10   particles was subjected to two successive rounds of 3D classification. A subset of

11   150,000 particles was used for further 3D refinements yielding a final map at 4.4 Å

12   resolution.

13   Both cleaned datasets were merged, corresponding to 1,109,475 particles from dataset

14   1 and 917,990 particles from dataset 2. Particles were subjected to 3D classification

15   with 3 classes. One class displayed the expected structural features of the AVP-V2R-Gs-

16   Nb35 complex corresponding to 877,003 particles and were selected for a new round of

17   3D classification with 6 classes. This classification revealed structural variability in the

18   ligand location and at the interface between the receptor and the Gs protein. Three

19   subsets of particles were selected (L, T1 and T2 states), re-extracted with a pixel size of

20   1.62 Å or 0.81 Å, and subjected to 3D refinements yielding maps at 4.5 Å, 4.7 Å and 5.5 Å

21   respectively. New rounds of 3D refinements were performed in applying a mask to

22   exclude both the micelle and the GαsAH yielding maps at 4.23 Å, 4.4 Å and 4.7 Å. CTF

23   refinement and polishing steps were applied on the three subsets of particles, allowing

24   us to improve the resolution of the best map to 4.17 Å (FSC = 0.143). The 1.62 Å/pixel

25   T1 map was resampled at 0.81 Å/pixel for visualization purposes. Final refinements

1   were processed with the option masking individual particles with zero turned-off. All

2   our attempts to refine our final subsets in cisTEM[45] and cryoSPARC[46] using non-uniform

3   refinement did not improve the resolution of final maps.

4   To investigate the conformational dynamics of the signalling complex, multi-body

5   refinement was performed on 877,003 particles, with two bodies corresponding to AVP-

6   V2R and Gs-Nb35. Local resolution was estimated with the Bsoft 2.0.3 package[47,48]. Map

7   sharpening was re-evaluated with Phenix autosharpen tool[49]. Phenix resolve_cryoEM

8   tool[16] was used to improve the map interpretability and allowed to increase the

9   estimated resolution to 4.04, 4.13 and 4.5 Å for L, T1 and T2 states, respectively

10   (**Supplementary Fig. 3**).

11

12   **Model building and refinement**

13   *Receptor and AVP initial models*

14   The V2R was built by comparative modelling, using the MODELLER software[50] and the

15   X-ray structure of the δ-opioid receptor at 3.4 Å resolution (PDB:4EJ4) as a template[51],

16   sharing a sequence similarity of about 44% with the V2R (on the modeled region).

17   Because modelling loops or terminal regions is a very challenging task and their

18   dynamical behavior is very poorly described in CG simulations, N- and C-terminus of the

19   receptor (residues 1-35 and 335-371, respectively) as well as part of the icl3 loop (237-

20   262) were lacking in the used template. Thus, only residues 36 to 236 and 263 to 334

21   were modeled. 500 models were generated and the one sharing the best objective

22   function score was further selected as a starting point for the simulations. The disulfide

23   bridge conserved among the class A GPCRs was included between residues 112 and 192

24   of the V2R.

1   The AVP peptide (NH_3^+-CYFQNCPRG-$CONH_2$) was built from its X-ray structure available

2   in the PDB (code 1JK4, 2.3 Å resolution) which describes the 6-residues cycle of the

3   peptide in interaction with neurophysin[52]. As depicted in **Supplementary Fig. 4** this

4   structure shows a cycle conformation equivalent to that found in bound (PDB code:

5   1NPO) and unbound related peptide oxytocin (PDB code: 1XY2)[53,54]. It was thus

6   preferred to the one describing the trypsin:vasopressin complex (PDB code : 1YF4)[55]

7   harboring a completely different conformation of the cycle. The three last residues of the

8   peptide ($_7$-PRG-$_9$) were also built with the oxytocin structure templates.

9   The obtained initial models of both receptor and peptide were then converted to a CG

10   representation using the MARTINI forces field (version 2.2, Elnedyn)[56]. Using such a

11   model, residues (backbone beads) closer than 9.0 Å are bound by a spring displaying a

12   force constant of 500 $kJ.mol^{-1}.nm^{-2}$ (default value from the Elnedyn force field). Such a

13   link is meant to maintain both the secondary and the tertiary structures of the

14   polypeptides. The resulting elastic networks of both the peptide and the receptor are

15   represented in **Supplementary Fig. 4**. For the peptide, only the springs involving two

16   residues of the cycle were conserved for further calculations, the three last residues

17   being free to move. The standard elastic network of the receptor was not modified and

18   allowed the latter to open or close freely as no spring was bridging the extracellular

19   loops.

20   *MD simulations*

21   The receptor was inserted in a 100x100 $Å^2$ lipid bilayer exclusively composed of POPC.

22   To avoid the exploration by the peptide of the intracellular side of the membrane during

23   MD (because of periodic boundary conditions), the system was duplicated/rotated along

24   the z-axis (the two extracellular sides of the receptors were facing each other), in order

25   to create an extracellular compartment. Two copies of the peptide were added to

1   increase the interaction sampling with a 1:1 ratio. In a last step, water and chloride

2   counter-ions were added to neutralize the system. The fully-solvated system included

3   20004 beads. A representation of the simulated box with two receptors and two

4   peptides is reported in Supplementary Fig. 3**.** After 10 000 steps of energy minimization

5   using the conjugate gradient algorithm, the system was further equilibrated at 51

6   different temperatures (in the range 300:450 K by steps of 3 K) in the NVT ensemble,

7   using an integration step of 20 fs and over a period of 5 ns. The final production step

8   was performed in the NPT ensemble, using an integration step of 20 fs and was stopped

9   after 20 μs. During production, Replica-Exchange MD (REMD) was used to improve the

10   sampling of all possible configurations of the peptide:receptor complex. The potential

11   energy difference of adjacent replicas was computed every 1000 steps (20 ps) and their

12   coordinates were exchanged according to a Boltzmann criterion. With the used

13   parameters, the probability of exchange between adjacent replica was in the range 0.11

14   (300K):0.23(450K). Three independent CG-REMD simulations were run to verify the

15   convergence of the obtained models, together representing a cumulated sampling time

16   of ~3 ms (**Supplementary Fig. 5**). For each of these simulations, a clustering was

17   performed on all conformations of the peptide:receptor complex obtained at the lowest

18   temperature (300 K). To do so, we first concatenated the data corresponding to the four

19   possible complexes (peptide1:receptor1, peptide1:receptor2, peptide2:receptor1 and

20   peptide2:receptor2). For that step, only the conformations displaying at least one

21   peptide:receptor contact were kept (a contact was defined using a cut-off distance of 7

22   Å). For clustering, we used the algorithm of Daura *et al.*[57] with a RMSD cut-off of 3.0 Å.

23   The RMSD was computed only on the backbone beads of the peptide's residues 1 to 6

24   after structural fit onto those of the V2R. The two cysteines side-chains beads were also

24

1   included for RMSD calculations. All simulations and analyzes were performed with the

2   Gromacs software (version 5)[58]. Figures were produced with VMD[59].

3   *Refinement of the obtained CG-models in the cryo-EM maps*

4   The Correlation-Driven Molecular Dynamics (CDMD) method[60] was employed to refine

5   the most populated clusters obtained in CG-REMD using the L state cryo-EM map of the

6   AVP-V2-Gs-Nb35 complex. The principle of the method is to use an accurate force field

7   and thermodynamic sampling to improve the real-space correlation between the

8   modeled structure and the cryo-EM maps. Before this refinement step, the Gs

9   heterotrimer and the Nb35 were modeled using the structure of the β2AR-Gs-Nb35

10 complex[40] as a reference. The MARTINI force field restrained the internal conformations

11 of the different partners with an internal elastic network. To increase significantly the

12 conformational plasticity of the receptor and explore new conformations specific to the

13 V2R, we modified its default elastic network. We automatically deleted the "long-range"

14 springs involving two beads whose indexes differ by at least 15. This contributed to

15 delete all inter-helices springs. The resulting elastic network used at this step for the

16 receptor is reported in **Supplementary Fig. 4**. The standard elastic network was

17 conserved for all other partners including the AVP peptide, the G protein and the Nb35.

18 No inter-chains springs were included for the G protein. After conversion of Gs and

19 Nb35 into the CG model, the two proteins were placed at a rational position in respect to

20 the V2R using the β2AR-Gs-Nb35 complex[40]. The full system was inserted in a larger

21 membrane (150x150 $Å^2$) and solvated on each side for further calculations.

22 The fit in each cryo-EM maps was performed in four successive steps summarized in

23 **Supplementary Fig. 6**. First, a quick energy minimization (2000 steps of conjugate

24 gradient) was performed on the full system without taking the map into account. This

25 step was dedicated to the removal of bad contacts resulting from the addition of Gs and

25

1 Nb35 proteins. Then the second step consisted in a first equilibration of 5 ns (10 fs time-

2 step; NVT; 300 K) performed with CDMD and using a constant targeted low resolution of

3 5 Å together with a strength constant of 10000 kJ.mol^{-1} for the map potential. This bias

4 was applied only to the backbone beads of the system. This step was useful to quickly

5 optimize the alignment of the system with the targeted map. During this second step, an

6 additional force of 50000 kJ.mol^{-1}.nm^{-2} was added to keep the distance between the two

7 centers of masses (COMs) of both the peptide and surrounding residues of the receptor

8 close to its initial value. This force prevented a quick motion of the AVP peptide in the

9 first steps of the simulation that resulted from large forces applying to the receptor. For

10 the subsequent steps of the fitting procedure, this additional force on COMs was

11 removed. During the step 3 (30 ns), the same MD parameters were used but with a

12 gradual increase of both the resolution (from 5 to 3 Å) and the strength constant (from

13 10000 to 50000 KJ.mol^{-1}), over a period of 25 ns. During the last 5 ns these values were

14 kept constant. This step was the key step allowing the whole system to adapt and fit to

15 the maps. Finally, the last step (10 ns) consisted in keeping the resolution and the

16 strength constant at their reached values (3 Å; 50000 KJ.mol^{-1}), but this time applying

17 the force only to the backbone and side-chain beads of the peptide. All the other

18 backbone beads of the system were restrained in positions during this step with a force

19 constant of 5000 KJ.mol^{-1}. This step was useful to refine the position of the peptide in the

20 density, especially of its side-chains. For every step of the fitting procedure, the fit of

21 each cluster was performed 5 times to verify the convergence of the obtained models

22 (**Supplementary Fig. 7**).

23

24 *All-atom refinement of the models in the maps*

1   The CG-models obtained from the fitting procedure were back-mapped to a full-atom

2   representation. We used the standard "initram" procedure provided by the developers

3   of Martini[61] with subtle changes. These changes concerned restrains on omega angles

4   and Cα-positions for all chains (V2R, Gs, Nb-35), to keep omega angles in trans

5   conformation and avoid large backbone motions which inevitably would lead to models

6   out of cryo-EM maps. Those restrains were added during the minimization and the MD

7   simulations inherent to the default "initram" procedure. In practice, the "initram"

8   procedure was as follow: 1/ after the very raw guess of atomic positions, from CG-beads,

9   done by the "initram" script, 2/ the Charmm36 force field[62] was used for 10000 steps of

10 steepest descent disabling the non-bonded terms, 3/ followed by 5000 steps of steepest

11 descent including all terms of the force field, and finally 4/ 300 steps of MD were

12 performed. Except the number of steps, the parameters for minimization and MD

13 simulations were set as default from the "initram" procedure. Minimization and MD

14 simulations were performed using the Gromacs package[58].

15 As a final step, iterative manual adjustments were carried out in COOT[63], and real space

16 refinement using Phenix programs[64]. The model statistics were validated using

17 Molprobity[65].

18

19 **Classical all-atom molecular dynamics simulations**

20 The L state cryoEM structure was subjected to molecular dynamics simulations (MDS).

21 The procedure is described in Supplementary Methods.

22

23 **NMR data analysis**

24 The purified V2R was prepared either in neutral amphipol (NAPol)[66,67] or in LMNG

25 detergent. In both cases, the V2R was expressed in Sf9 insect cells and purified as

27

1 described above, except it was cleaved overnight at 4°C using the HRV3C protease at a

2 1:20 weight ratio (HRV3C:V2R) before concentration and purification by SEC.

3 1D STD NMR spectra[68] were recorded either on a mixture of AVP with V2R (400

4 μM:2 μM), or on AVP (**Supplementary Fig. 8**). Selective methyl resonance saturation

5 was achieved by equally spaced 60 ms Gaussian 180° pulses separated by 1 ms delay at

6 0 ppm (−50 ppm for reference spectra) at 274K and 283K. An irradiation test was

7 performed on a free peptide sample (400 μM) to verify that only V2R resonances were

8 irradiated. Subtraction of free induction decay with on- and off-resonance protein

9 saturation was achieved by phase cycling. A relaxation delay of 2.6s (Aq+D1) and 128

10 dummy scans were employed to reduce subtraction artifacts. Investigation of the time

11 dependence of the saturation transfer from 0.5 to 4 s with equally spaced 50-ms

12 Gaussian shaped pulses (separated by a 1-ms delay) showed that 2 s was needed for

13 efficient transfer of saturation from V2R to the AVP. A T1ρ filter of 30 ms was applied to

14 eliminate background resonances of V2R. The transient number was typically 4k. To

15 determine the specificity of STD signals, similar samples were prepared with the

16 antagonist TVP as competitor, using 3 μM V2R, 80 μM AVP and 550 μM TVP. The STD

17 effect was then calculated as $(I_0-I_{sat})/I_0$ where I_0 and I_{sat} are the intensities of one signal

18 in the reference NMR spectrum and in the on-resonance spectrum, respectively.

19 We discriminated the different molecular models issued from CG-MD simulations by

20 comparing the experimental STD values and the expected simulated STD from model

21 structures. Back calculation of STD intensities were calculated with the 3.8 version of

22 CORCEMA-ST software[69]. An order parameter value of 0.85 for methyl groups, and a Kon

23 value of a 10^8 s^{-1} value were used. The correlation times were set to 0.5 and 40 ns for the

24 free and bound states respectively. Calculations with different correlation time values

25 exploring the 0.2-2 ns and 10-30 ns for the free and bound forms, respectively, showed

1   that the simulated profiles, and in particular the correlation coefficient between

2   calculated and experimental values, were much more dependent on the template model

3   than on the correlation time values. Coefficient correlations between simulated and

4   experimental values were calculated for the whole peptide (residues 1-9). Mean

5   correlations factors R_{1-9} were calculated for five representative structures of each

6   cluster.

7

8   **TR-FRET binding assays**

9   V2R binding studies using TagLite® assays (Cisbio, Codolet, France) based on time-

10 resolved-FRET measurements were previously described[70,71]. These are detailed in

11 Supplementary Methods.

12

13 **cAMP accumulation assays**

14 As for V2R binding studies, V2R functional studies based on time-resolved FRET

15 measurements were described previously[39,26]. These are detailed in Supplementary

16 Methods.

17

18 **Data Availability**

19 The cryo-EM density maps for the AVP-V2R-Gs-Nb35 complex have been deposited in

20 the Electron Microscopy Data Bank (EMDB) under accession code EMD-12128 (L state)

21 and EMD-12129 (T state). The coordinates for the models of AVP-V2R-Gs-Nb35 complex

22 have been deposited in the PDB under accession numbers 7BB6 and 7BB7 (L and T

23 states, respectively). We declare that the data supporting findings for this study are all

24 available upon request to the corresponding authors.

25

1 **References**

2 38. Morello, J. P., Bouvier, M., Petäjä-Repo, U. E. & Bichet, D. G. Pharmacological

3   chaperones: A new twist on receptor folding. *Trends Pharmacol. Sci.* **21**, 466–469

4   (2000).

5 39. Jean-Alphonse, F. *et al.* Biased agonist pharmacochaperones of the AVP V2

6   receptor may treat congenital nephrogenic diabetes insipidus. *J. Am. Soc. Nephrol.*

7   **20**, 2190–2203 (2009).

8 40. Rasmussen, S. G. F. *et al.* Crystal structure of the human β2 adrenergic G-protein-

9   coupled receptor. *Nature* **450**, 383–387 (2007).

10 41. Mastronarde, D. N. Automated electron microscope tomography using robust

11   prediction of specimen movements. *J. Struct. Biol.* **152**, 36–51 (2005).

12 42. Zivanov, J. *et al.* New tools for automated high-resolution cryo-EM structure

13   determination in RELION-3. *Elife* **7**, 1–39 (2018).

14 43. Zhang, K. Gctf: Real-time CTF determination and correction. *J. Struct. Biol.* **193**, 1–

15   12 (2016).

16 44. Tegunov, D. & Cramer, P. Real-time cryo-EM data pre-processing with Warp.

17   *bioRxiv* 338558 (2018) doi:10.1101/338558.

18 45. Grant, T., Rohou, A. & Grigorieff, N. cisTEM, user-friendly software for single-

19   particle image processing. *Elife* **7**, (2018).

20 46. Punjani, A., Rubinstein, J. L., Fleet, D. J. & Brubaker, M. A. CryoSPARC: Algorithms

21   for rapid unsupervised cryo-EM structure determination. *Nat. Methods* **14**, 290–

22   296 (2017).

23 47. Heymann, J. B. Guidelines for using Bsoft for high resolution reconstruction and

24   validation of biomolecular structures from electron micrographs. *Protein Sci.* **27**,

25   159–171 (2018).

1 48. Cardone, G., Heymann, J. B. & Steven, A. C. One number does not fit all: mapping

2   local variations in resolution in cryo-EM reconstructions. *J. Struct. Biol.* **184**, 226–

3   36 (2013).

4 49. Terwilliger, T. C., Sobolev, O. V, Afonine, P. V & Adams, P. D. Automated map

5   sharpening by maximization of detail and connectivity. *Acta Crystallogr. Sect. D,*

6   *Struct. Biol.* **74**, 545–559 (2018).

7 50. Webb, B. & Sali, A. Protein Structure Modeling with MODELLER. *Methods Mol. Biol.*

8   **1654**, 39–54 (2017).

9 51. Granier, S. *et al.* Structure of the δ-opioid receptor bound to naltrindole. *Nature*

10   **485**, 400–404 (2012).

11 52. Wu, C. K. *et al.* Structures of an unliganded neurophysin and its vasopressin

12   complex: Implications for binding and allosteric mechanisms. *Protein Sci.* **10**,

13   1869–1880 (2001).

14 53. Rose, J. P., Wu, C., Hsiao, C., Breslow, E. & Wang, B. Crystal structure of the

15   neurophysin-oxytocin complex. *Nat. Struct. Biol.* **3**, 163–169 (1996).

16 54. Schmidt, J. M. *et al.* Conformation of [8-arginine]vasopressin and V1 antagonists in

17   dimethyl sulfoxide solution derived from two-dimensional NMR spectroscopy and

18   molecular dynamics simulation. *Eur. J. Biochem.* **201**, 355–71 (1991).

19 55. Ibrahim, B. S. & Pattabhi, V. Trypsin inhibition by a peptide hormone: Crystal

20   structure of trypsin-vasopressin complex. *J. Mol. Biol.* **348**, 1191–1198 (2005).

21 56. Marrink, S. J., Risselada, H. J., Yefimov, S., Tieleman, D. P. & De Vries, A. H. The

22   MARTINI force field: Coarse grained model for biomolecular simulations. *J. Phys.*

23   *Chem. B* **111**, 7812–7824 (2007).

24 57. Daura, X., Jaun, B., Seebach, D., van Gunsteren, W. F. & Mark, A. E. Reversible

25   peptide folding in solution by molecular dynamics simulation. *J. Mol. Biol.* **280**,

1 925–932 (1998).

2 58. Abraham, M. J. *et al.* Gromacs: High performance molecular simulations through

3   multi-level parallelism from laptops to supercomputers. *SoftwareX* **1–2**, 19–25

4   (2015).

5 59. Humphrey, W., Dalke, A. & Schulten, K. VMD: visual molecular dynamics. *J. Mol.*

6   *Graph.* **14**, 33–38 (1996).

7 60. Igaev, M., Kutzner, C., Bock, L. V, Vaiana, A. C. & Grubmüller, H. Automated cryo-EM

8   structure refinement using correlation-driven molecular dynamics. *Elife* **8**, (2019).

9 61. Wassenaar, T. A., Pluhackova, K., Böckmann, R. A., Marrink, S. J. & Tieleman, D. P.

10   Going Backward: A Flexible Geometric Approach to Reverse Transformation from

11   Coarse Grained to Atomistic Models. *J. Chem. Theory Comput.* **10**, 676–90 (2014).

12 62. Best, R. B. *et al.* Optimization of the additive CHARMM all-atom protein force field

13   targeting improved sampling of the backbone φ, ψ and side-chain χ(1) and χ(2)

14   dihedral angles. *J. Chem. Theory Comput.* **8**, 3257–3273 (2012).

15 63. Emsley, P. & Cowtan, K. Coot: Model-building tools for molecular graphics. *Acta*

16   *Crystallogr. Sect. D Biol. Crystallogr.* **60**, 2126–2132 (2004).

17 64. Afonine, P. V *et al.* Joint X-ray and neutron refinement with phenix.refine. *Acta*

18   *Crystallogr. D. Biol. Crystallogr.* **66**, 1153–63 (2010).

19 65. Chen, V. B. *et al.* MolProbity: all-atom structure validation for macromolecular

20   crystallography. *Acta Crystallogr. D. Biol. Crystallogr.* **66**, 12–21 (2010).

21 66. Sharma, K. S. *et al.* Non-ionic amphiphilic homopolymers: synthesis, solution

22   properties, and biochemical validation. *Langmuir* **28**, 4625–39 (2012).

23 67. Rahmeh, R. *et al.* Structural insights into biased G protein-coupled receptor

24   signaling revealed by fluorescence spectroscopy. *Proc. Natl. Acad. Sci. U. S. A.* **109**,

25   6733–6738 (2012).

1 68. Mayer, M. & Meyer, B. Characterization of ligand binding by saturation transfer

2   difference NMR spectroscopy. *Angew. Chemie - Int. Ed.* **38**, 1784–1788 (1999).

3 69. Krishna, N. R. & Jayalakshmi, V. Quantitative Analysis of STD-NMR Spectra of

4   Reversibly Forming Ligand-Receptor Complexes. *Top Curr Chem* **273**, 15–54

5   (2008).

6 70. Zwier, J. M. *et al.* A fluorescent ligand-binding alternative using Tag-lite®

7   technology. *J. Biomol. Screen.* **15**, 1248–59 (2010).

8 71. Loison, S. *et al.* Selective fluorescent nonpeptidic antagonists for vasopressin V_2

9   GPCR: application to ligand screening and oligomerization assays. *J. Med. Chem.*

10   **55**, 8588–602 (2012).

11

12

13

14

10

11   **Author contributions** J.B. purified V2R and AVP-V2R-Gs-Nb35 complexes, screened

12   samples by negative staining EM and cryo-EM, prepared grids, collected and processed

13   cryo-EM data, generated the cryo-EM maps and built some Extended data Figures. H.O.

14   managed the Sf9 cell culture and baculoviral infections, expressed and purified V2R,

15   purified AVP-V2R-Gs-Nb35 complexes, prepared grids for cryo-EM. N.F. developed the

16   CG-REMD modelling approach, fitted the models onto the cryo-EM maps and back-

17   mapped the models to all-atom representation. C.L. built the final models of AVP-V2R-

18   Gs-Nb35 complexes into cryo-EM and performed MD simulations. J. L-K-H and A. A.

19   screened samples by negative staining EM and prepared grids for cryo-EM. G.G.

20   contributed to the expression and purification of V2R. J. S-P expressed and purified Gs

21   protein and Nb35 nanobody. S.T. contributed to processing cryo-EM data for generating

22   cryo-EM maps. M.L. contributed to CG-REMD molecular dynamics modelling. S.G.

23   established all the initial procedures for the ternary complex purification. R.S. designed

24   Gs constructs, expressed and purified Gs protein and built most of the Figures. H.D.

25   managed STD NMR experiments and generated the STD NMR data. B.M. designed the

1   V2R construct and determined its pharmacological properties with the help of H.O. S.G.

2   P.B. and B.M. wrote the paper with the input from J.B., N.F. and H.D. Finally, S.G., P.B and

3   B.M. supervised the project.

4

5   **Competing interests**

6   The authors declare no competing interests.

7

8   **Additional information**

9   **Supplementary information** is available in the online version of the paper.

10   **Correspondence and requests for materials** should be addressed to S.G, P.B or B.M.

11

12

Figure 1 | Overview of the hybrid strategy: a combination of cryo-EM, computational and NMR.

a

CG-REMD 1

b Cluster 1 Cluster 2 Cluster 3 Cluster 4 Cluster 5

(25 %) (8 %) (6.5 %) (5 %) (5 %)

Cluster 6 Cluster 7 Cluster 8 Cluster 9 Cluster 10

(4.5 %) (4 %) (4 %) (3 %) (2.5 %)

c **EM FIT (Loose Map)**

step 1 step 2 step 3

d **STD NMR**

e

Agreement with NMR restraints

Agreement with EM map

mean r.m.s.d. (Å)

R_{1-9}

ReMapping (Loose Map) 3

f

g

EM FIT (Tight Map) 4
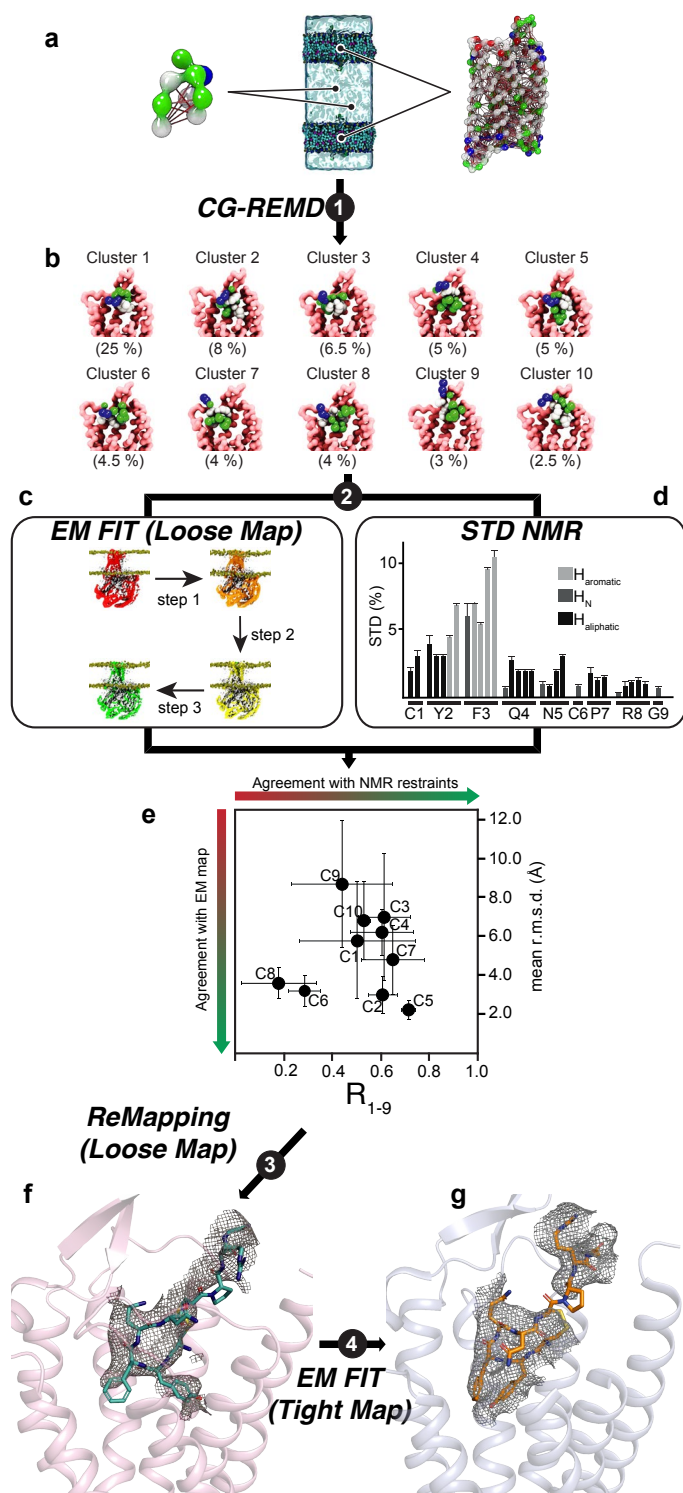
Fig. 1| Overview of the hybrid strategy: a combination of cryo-EM, computational and NMR. a) schematic representation of the unbiased CG ab-initio approach. The internal elastic networks used for both the AVP (left) and the V2R (right) are shown. The full system (centre) used for the CG-REMD simulations included two receptors and two peptides in order to create an artificial extracellular compartment and improve the conformational sampling. **b**) 10 most populated clusters obtained for the AVP-V2R complex after the 3 independent CG-REMD simulations. The upper parts of TM 6 and TM7 of V2R were removed for clarity. The 10 clusters describe 67.5% of the whole conformations analysed in the procedure. **c**) schematic representation of the successive steps employing the CDMD method to fit the models resulting from the CG-REMD simulations into the L cryo-EM map of the AVP-V2R-Gs-Nb35 complex. **d**) Mapping AVP contact surface by experimental STD NMR. The STD effect profile (in %) is shown as a function of AVP protons (aliphatic, N (backbone), aromatic). Intense STD signals were only observed in the presence of V2R, mostly for the aromatic protons of Tyr[2] and Phe[3] (and to a lesser extent of Cys[1]) residues of AVP. **e**) Cross-correlation between computational and STD NMR. First, variability of the position of AVP was calculated as mean RMSD values (in Å**)** after cross-comparison of models (5 for each cluster) resulting from the fitting procedure of each of the 10 clusters in the L density map. Cluster 5 showed the smaller variability (2.2 Å). Second, experimental STD values were compared to the expected STD values from all-atom models issued from MD simulations and correlation coefficients were calculated for the whole peptide (R_{1-9}). Cluster 5 appeared as the best cluster fitting to experimental STD values. **f**) Remapping into the L density map. Based on cluster 5, the final L model was then built in a more conventional manner to match as closely as possible the L density map. **g**) Based on the L model, the T model was built to match the T density map.

# Figure 2 | Structures of AVP-V2R-Gs-Nb35 complexes in L and T conformations.
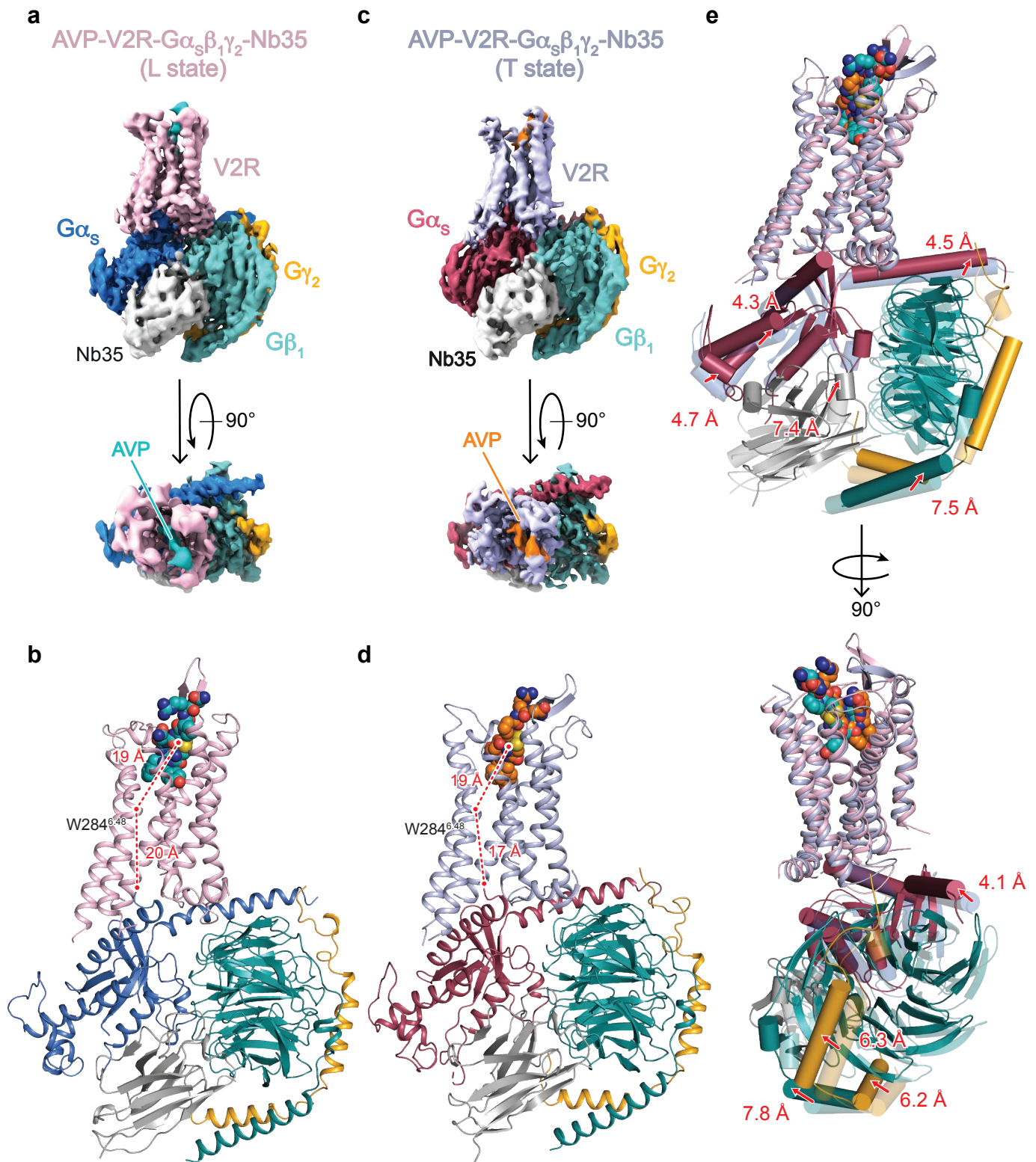
Fig. 2| Structures of AVP-V2R-Gs-Nb35 complexes in L and T conformations. a) orthogonal views of the cryo-EM density maps of the L state of the AVP-V2R-Gs-Nb35 complex and **b)** corresponding model as ribbon representation. V2R is coloured in pink, Gαs in dark blue, Gβ1 in turquoise, Gγ2 in yellow, Nb35 in grey, AVP in cyan. In **b**, the distances between W284[6.48] (at its Cα carbon) and the AVP center of mass, and between W284[6.48] and the C-terminal end of α5 helix of Gs (at the Cα carbon of the free carboxylic acid) are shown. **c)** and **d)** corresponding maps and model for the T state. V2R is coloured in blue grey, Gαs in raspberry, Gβ1 in turquoise, Gγ2 in yellow, Nb35 in grey, AVP in orange. In **d**, distances are measured as in **b**. **e)** L and T models are aligned on the V2R chains, and rotations/translations are shown by measuring displacement (in Å) of Gαs, Gβ1, Gγ2 and Nb35.

Figure 3 | AVP Binding site of the V2R, comparison with retosiban binding site in OTR.
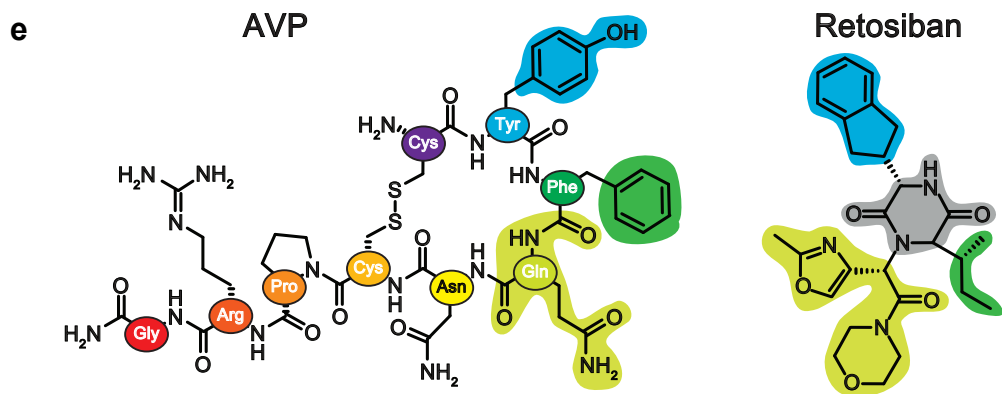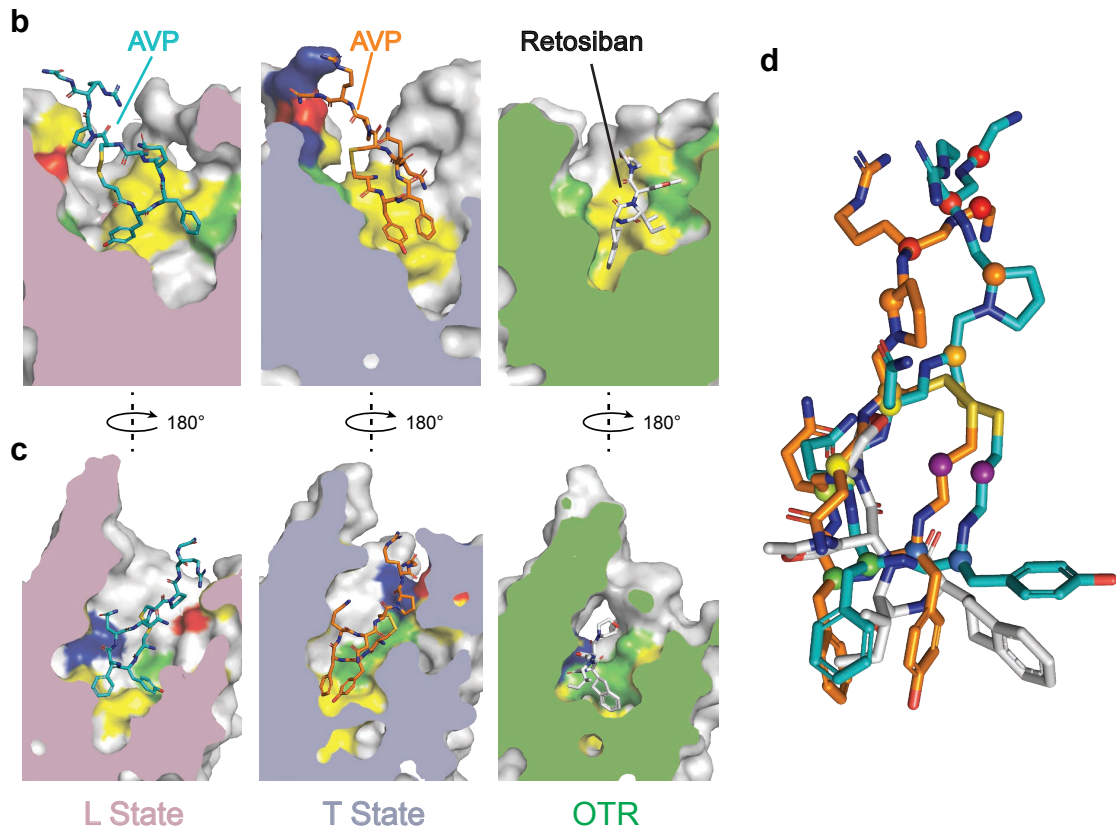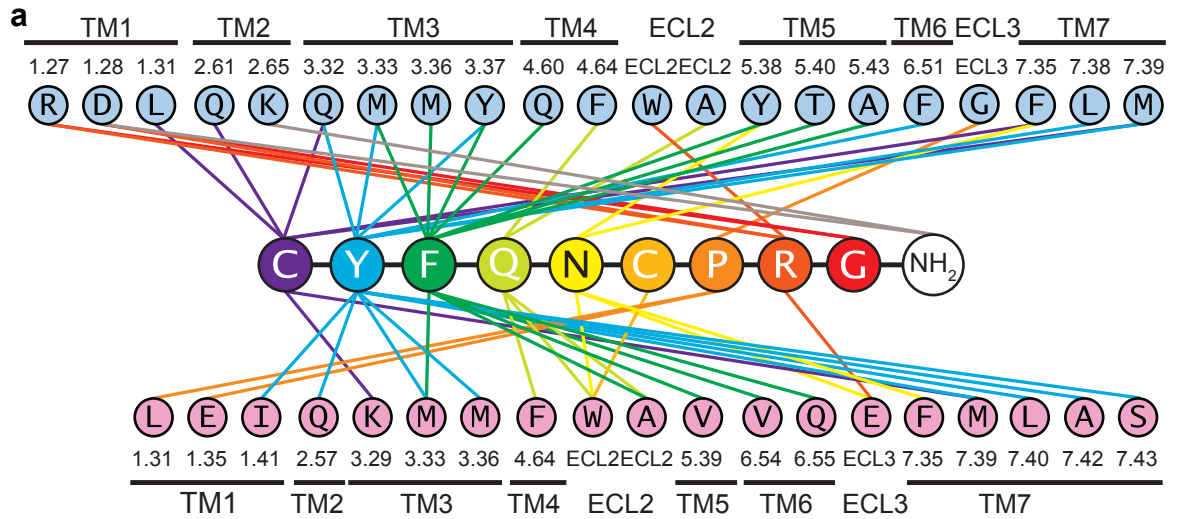
Fig. 3| AVP binding site of the V2R, comparison with retosiban binding site in OTR. a) Direct contacts between AVP and V2R in L and T structures. Interactions (within a maximum 5 Å distance) are shown between each AVP residue (and the C-terminal amide) with V2R residues in the L structure (pink) and in the T structure (blue). All TM helices and extracellular loop 2 and 3 interact with the hormone AVP. V2R residues are labeled according to the Ballesteros-Weinstein numbering. Each residue from AVP is colored differently for clarity. **b**) Side views of the binding pocket in the L and T structures and in the inactive structure of OTR. AVP binding modes in the L (pink) and T (light blue) structures, are compared to that of the small molecule antagonist retosiban in the OTR structure (green), all viewed from TM3. Residues from receptors that interact with AVP or retosiban are depicted in different colors:

yellow for hydrophobic, green for polar, red and dark blue for negatively and positively charged, respectively. **c**) Side views of the binding pockets after a 180° rotation. AVP and retosiban are viewed from TM6. The same color code is used. **d**) Superimposition of AVP and retosiban. The peptide agonist and the nonpeptide antagonist are superimposed after alignment of V2R and OTR structures. The most hydrophobic parts of both ligands superimpose at the bottom of the orthosteric binding pocket. **e**) Structure comparison of AVP and retosiban. AVP is shown using the same color code than in pannel a. The retosiban indanyl moiety, the sec-butyl group, and the oxazol-morpholine amide moiety superimpose with AVP Tyr2, Phe3 and Gln4 respectively. The retosiban 2,5-diketopiperazine core is positioned between AVP Tyr2 and Phe3.

Figure 4 | Active conformations of L and T V2R states, comparison with inactive structure of OTR and active/inactive structures of β2AR.
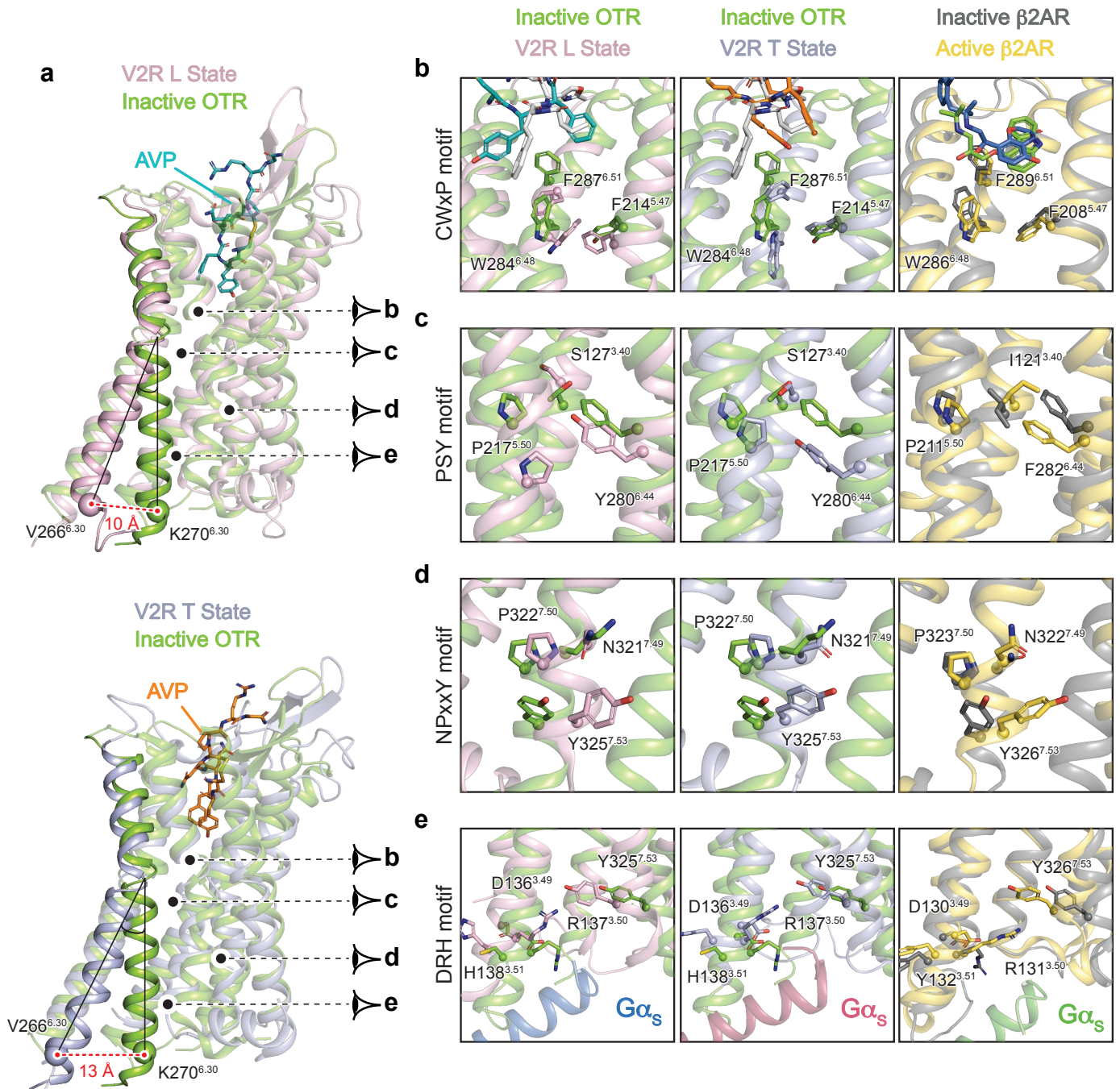

Fig. 4| Active conformations of L and T V2R states, comparison with inactive structure of OTR and active/inactive structures of β2AR. a) Large-scale displacement of TM6. The V2R L (pink) and T (blue grey) active structures are aligned onto that of the inactive OTR (green) structure. Residue 6.30 (Ballesteros-Weinstein numbering) is chosen as a reference (V266 in V2R, K270 in OTR) for measuring the outward movement of TM6: 10 and 13 Å between OTR and V2R in the L and T states, respectively. Activation of molecular switches along the helix bundle of the V2R are viewed in panels b, c, d and e. For comparison, rearrangements of those corresponding motifs in the β2AR are depicted. **b**) Rotameric toggle switch in the conserved CWxP motif. Position of $W^{6.48}$, $F^{6.51}$ and $F^{5.47}$ (284, 287 and 214 in V2R) are shown. **c**) Rearrangement of the PSY transmission switch. The $P^{5.50}$-$S^{3.40}$-$Y^{6.44}$ motif (217, 127 and 280 in V2R) is equivalent to the PIF motif in other GPCRs. **d**) Rotation of the NPxxY conserved motif in TM7. The conserved $Y^{7.53}$ (position 325 in V2R) is shown. **e**) Breaking of the conserved ionic lock in TM3. Upon activation of V2R, the ionic bond between $D136^{3.49}$ and $R137^{3.50}$ is broken and $R137^{3.50}$ projects to $Y325^{7.53}$.

# Figure 5 | Interface of the V2R T state with Gs
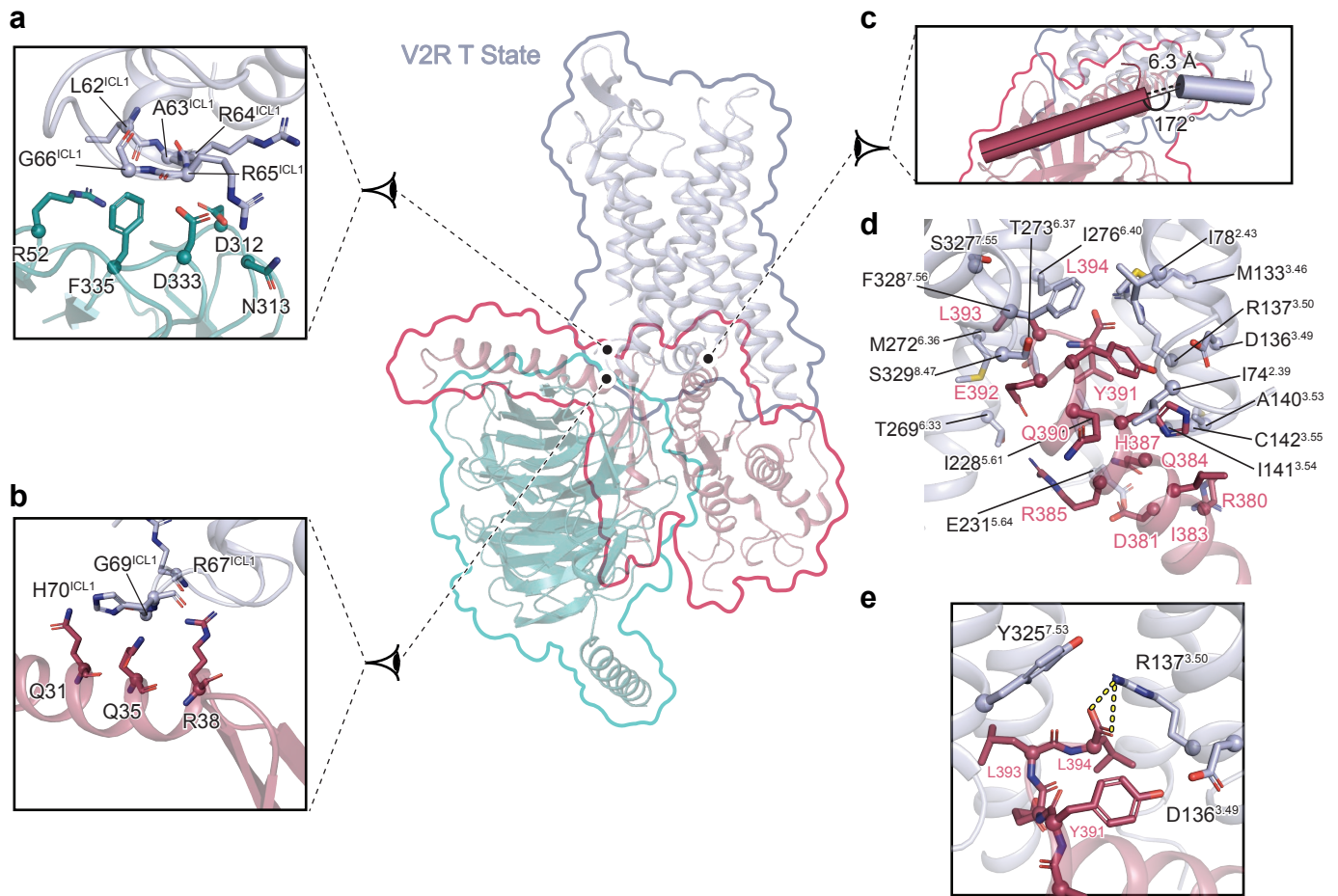
Fig. 5| Interface of the V2R T state with Gs.
Interactions between V2R and Gs heterotrimer are shown. Specific interfaces are depicted, and residues in close proximity (within a maximal 3.9 Å distance) are highlighted (blue grey for V2R, turquoise for Gβ subunit, raspberry for Gα subunit). **a**) Interaction of V2R ICL1 with Gβ subunit. **b**) Interaction of V2R ICL1 with N-terminal helix of Gα subunit. **c**) Position of C-terminal h5 helix of Gα subunit relative to V2R helix 8. The distance between Gα and helix 8 is indicated. Angle between these two domains is shown. **d**) Interacting residues between the C-terminal h5 helix of Gα subunit and V2R. **e**) Zoom on an ionic bridge between the C-terminal free carboxylic moiety of h5 helix of Gα subunit and V2R R137$^{3.50}$.

Extended Data Figure 1 | Overview of AVP-V2R-Gs-Nb35 complex preparation and purification.

a

b

c

d
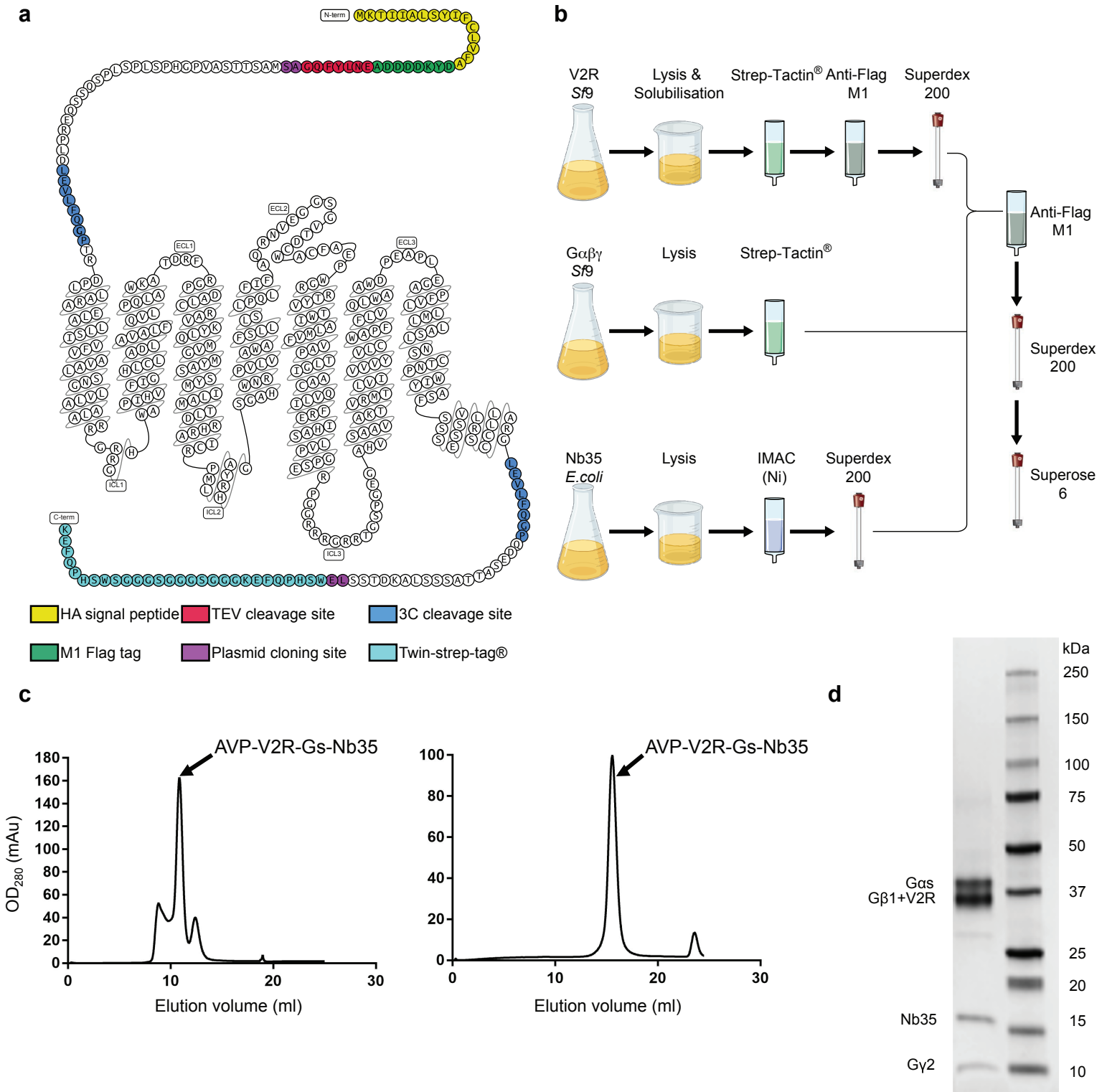
Extended data Figure 1 | Overview of AVP-V2R-Gs-Nb35 complex preparation and purification. a) Modified snake plot from https://gpcrdb.org of the engineered V2R construct used for cryo-EM structure determination. HA, hemagglutinin signal peptide; TEV protease, tobacco etch virus protease; 3C, human rhinovirus 3C protease; plasmid cloning sites are Nhe1 and Xho1 restriction sites. **b**) Workflow for AVP-V2R-Gs-Nb35 assembly. V2R receptor, Gs heterotrimer and Nb35 were expressed and purified separately, the complex being isolated by a final affinity chromatography and two successive SEC steps. **c**) Representative chromatograms of the AVP-V2R-Gs-Nb35 complex using Superdex200 and Superose6 SEC columns show a monodisperse peak. Fractions containing the sample were combined and concentrated for preparation of cryo-EM grids. **d**) SDS-PAGE of peak fraction from the Superose6 step. Coomassie blue staining of proteins confirmed that the complex is made of Gαs, V2R, Gβ1, Nb35 and Gγ2 (AVP is not visible).

# Extended Data Figure 2 | Cryo-EM workflow.
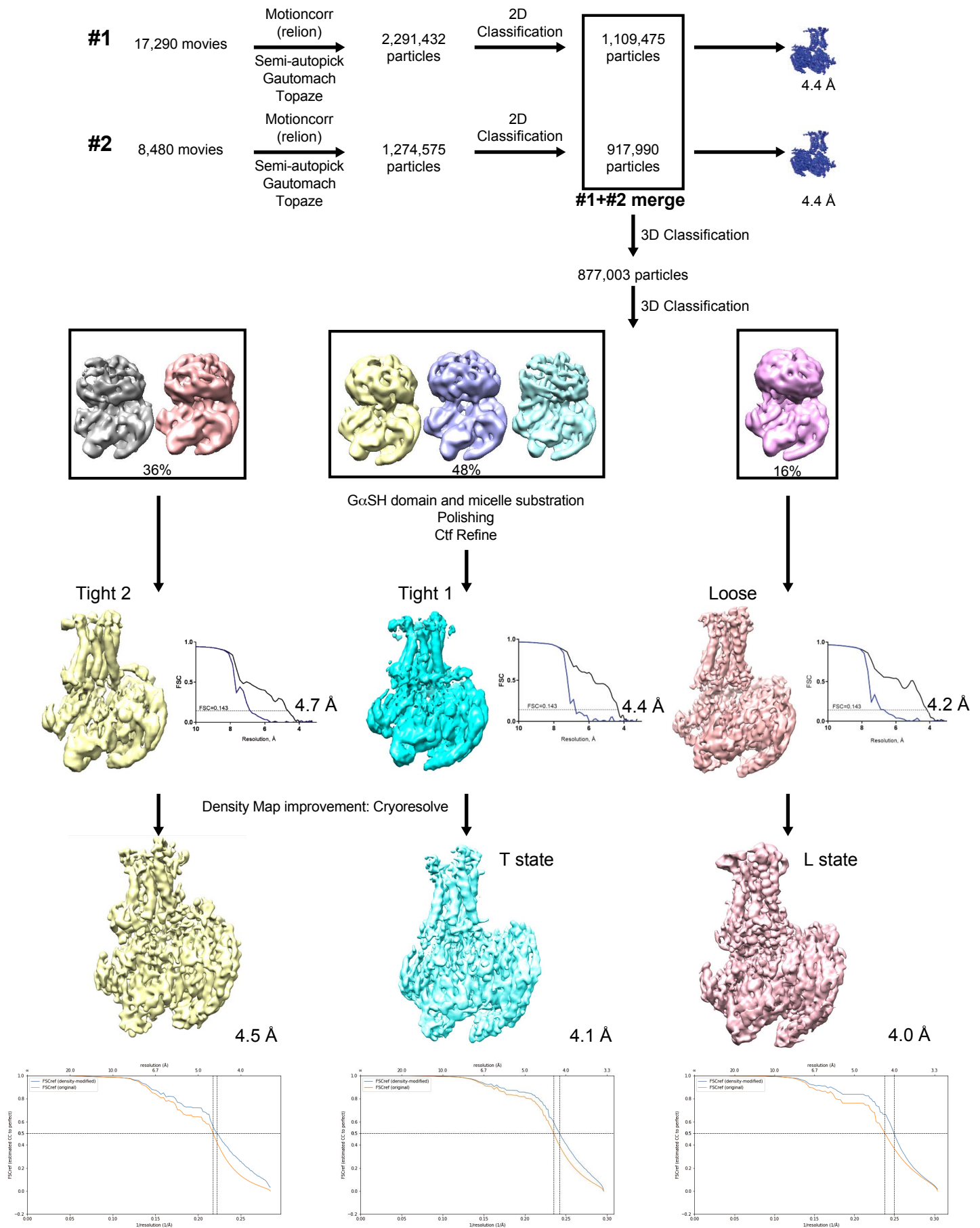
Extended data Figure 2 | Cryo-EM workflow. Flowchart of the single particle analysis for the two datasets processed separately. Merging of the two sets, substates determination and high-resolution reconstructions. Density map improvement with cryoresolve as a final step.

Extended Data Figure 3 | Cryo-EM characterization of the AVP-V2R-Gs-Nb35 complex.

a

c

3.2   4.0   4.8   5.6   6.4

b

d
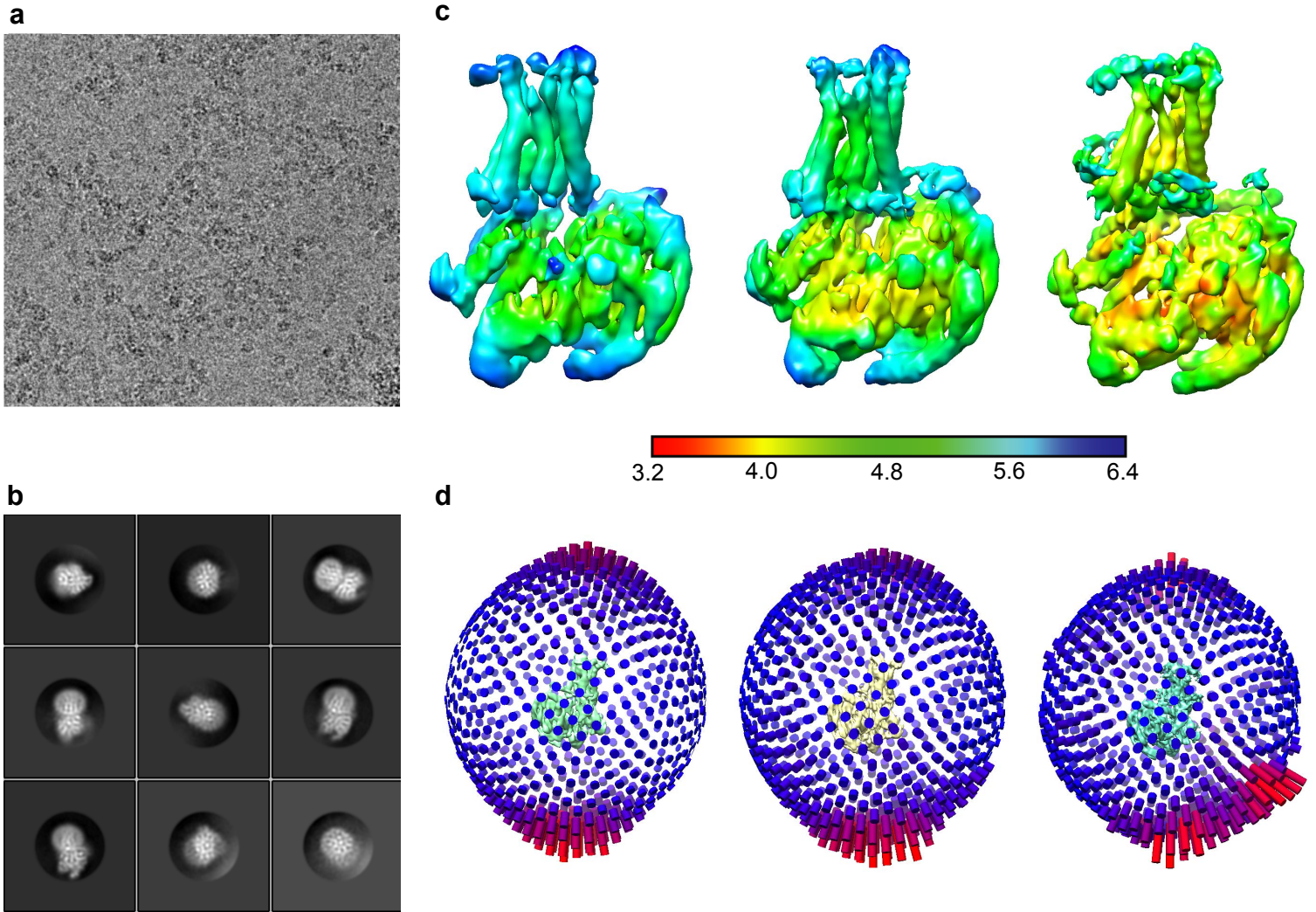
Extended data Figure 3 | Cryo-EM characterization of the AVP-V2R-Gs-Nb35 complex. a) Representative micrograph of the AVP-V2R-Gs-Nb35 protein complex (scale bar, 30 nm). **b**) Representative 2D class averages showing distinct secondary structure features (including the V2R TM regions embedded in the detergent micelle) and different orientations of the AVP-V2R-Gs-Nb35 complex (scale bar, 5 nm). **c**) Local resolution estimation computed with blocres from bsoft program; Tight-2, Tight-1 and Loose particle density maps are shown, respectively. **d**) Euler angle distribution of particles from the final reconstructions for Tight-2, Tight-1 and Loose populations.

**Extended Data Figure 4 | Flexibility in the AVP-V2R-Gs-Nb35 complex.**
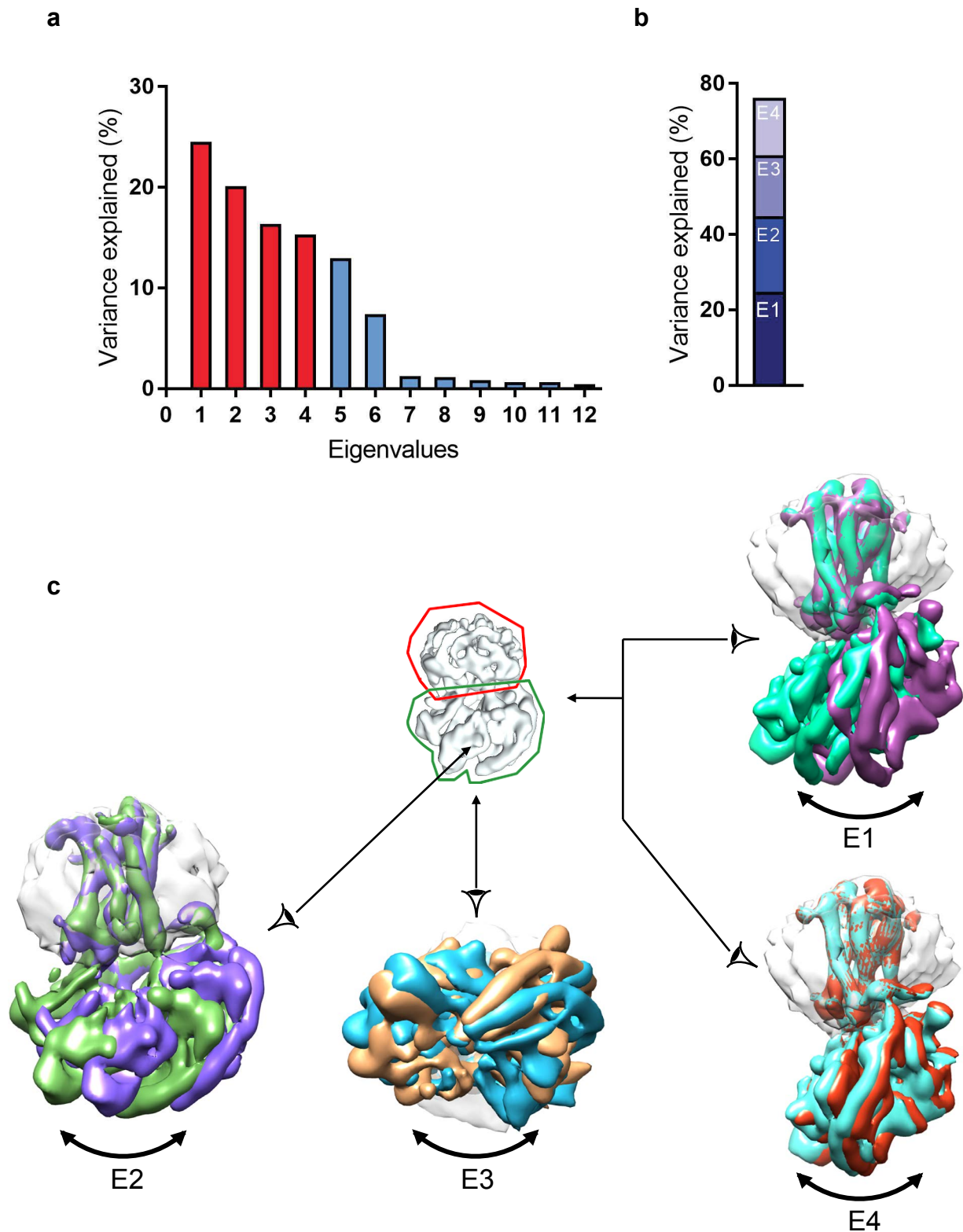
Extended data Figure 4 | Flexibility in the AVP-V2R-Gs-Nb35 complex. a) The contribution of each of the twelve eigen-vectors (numbered along x-axis) to the variance of the overall final map is illustrated. **b)** Eigenvectors 1 to 4 correspond to 78% of the variance. **c)** Mask employed for multi-body refinement is shown in the middle, detergent micelle and V2R are surrounded by a red line, Gs and Nb35 by a green line. Maps corresponding to the four first vectors are illustrated, showing swing-like motion and tilting of Gs-Nb35 with respect to AVP-V2R. E4 is part of E1.

Extended Data Figure 5 | Cryo-EM map quality for L and T states of the AVP-V2R-Gs-Nb35 complex.

a V2R L state
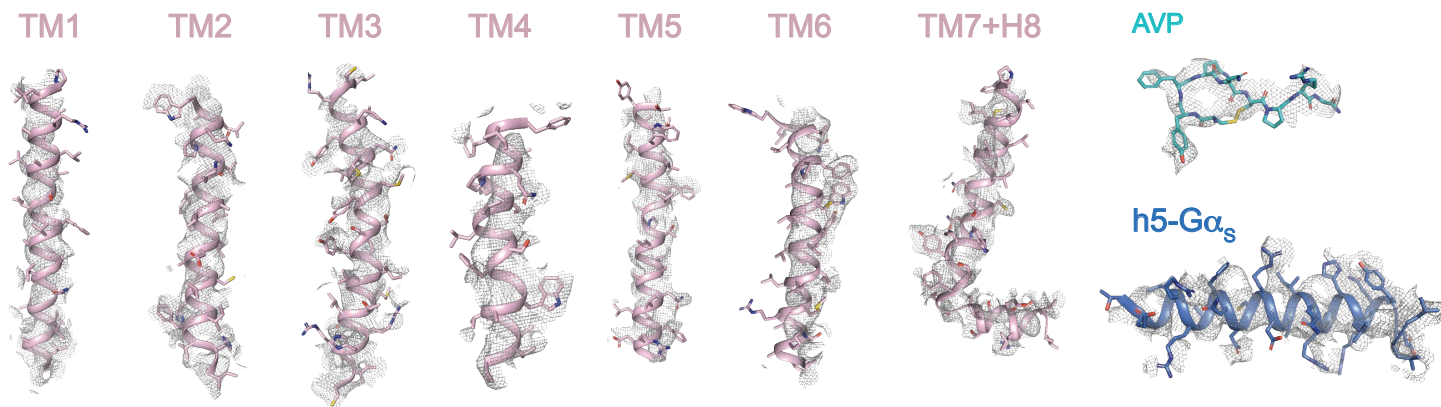
b V2R T state
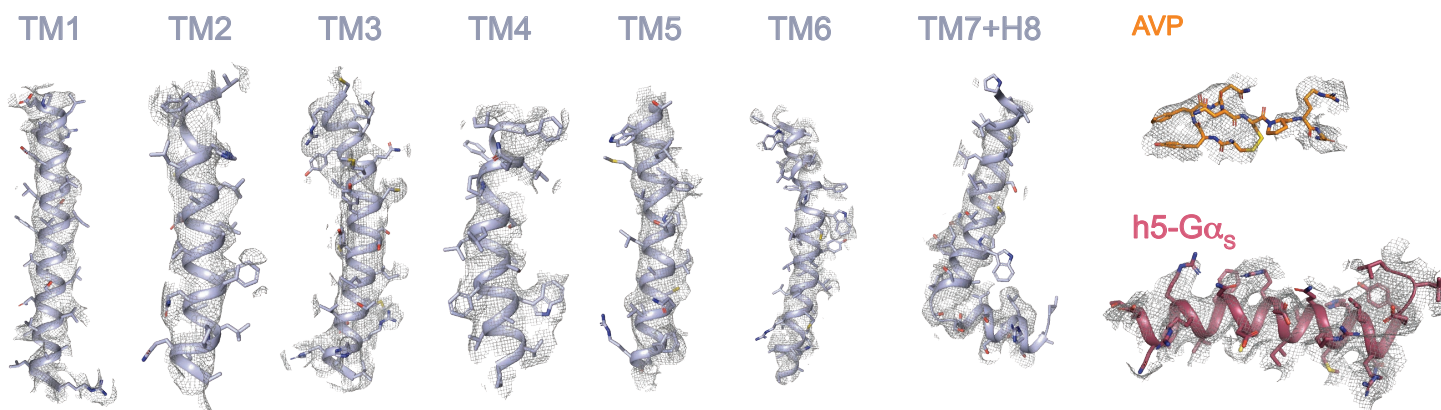
Extended data Figure 5 | Cryo-EM map quality for L and T states of the AVP-V2R-Gs-Nb35 complex. a) The density and model for TM helices 1-7 and helix H8 of V2R, α5 helix of Gαs and AVP in Loose (L) state. **b)** The density and model of corresponding protein domains and AVP in the Tight (T) state.

Extended Data Figure 6 | V2R and OTR Binding pockets : binding of AVP vs Retosiban.
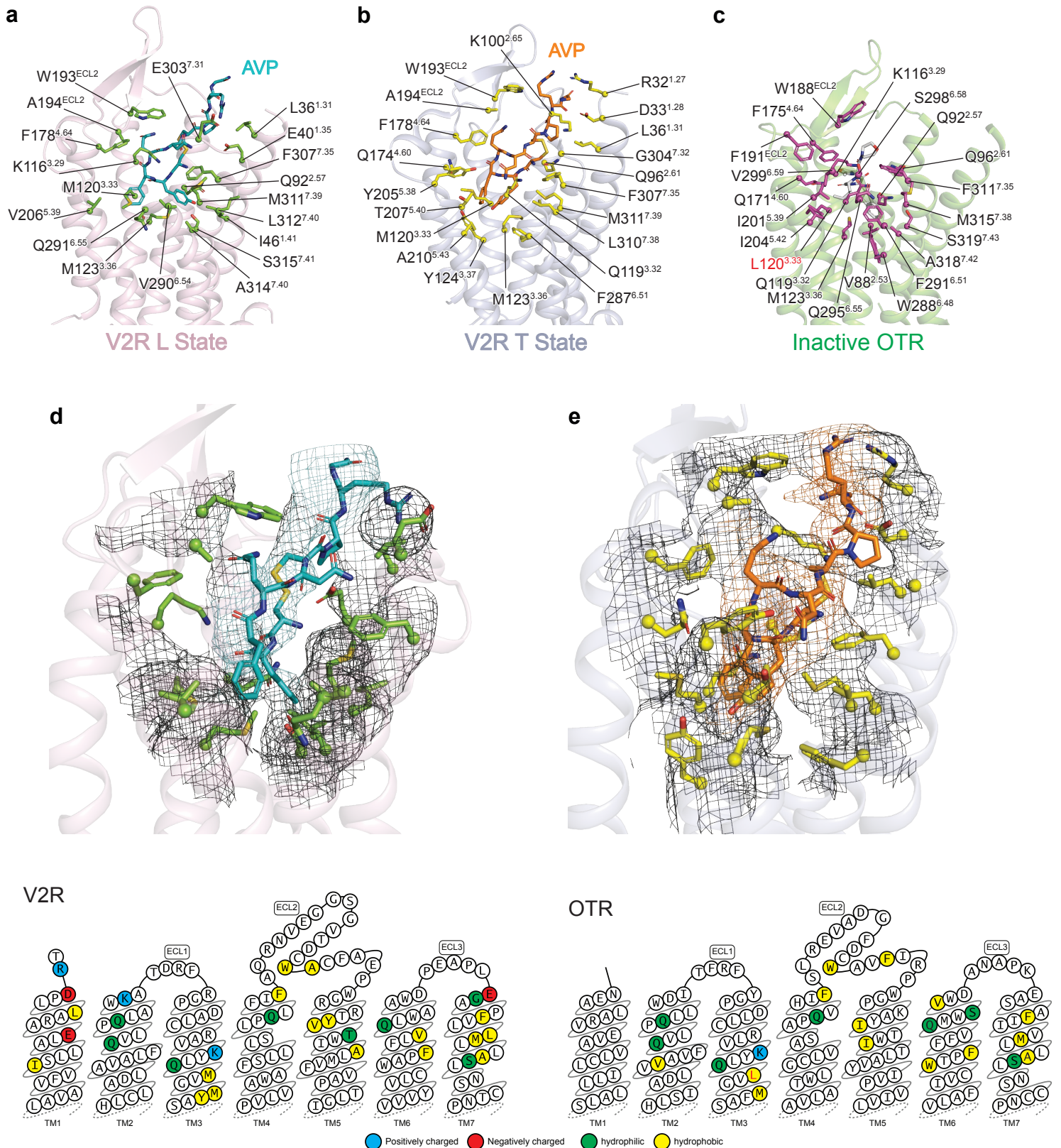
Extended data Figure 6 | V2R and OTR binding prockets: binding of AVP vs Retosiban. AVP binding poses are viewed from the side of V2R helix bundle in L (**a**), T (**b**) states and are compared with that of retosiban (in white sticks) in OTR (**c**). Receptor residues directly interacting with the ligands (at a maximum 5 Å distance) are indicated (Ballesteros-Weinstein numbering). In the OTR, L120[3.33] (highlighted in red) is a mutation introduced in the sequence to increase thermostability and facilitate crystallogenesis (V120L). Densities of V2R residues in contact with AVP are shown in L (**d**) and T states (**e**), respectively. **f**) Residues of V2R and OTR involved in the binding of ligands are shown in receptor snake-like plot representations (https://gpcrdb.org).

Extended data Figure 7 | Interface of the V2R L state with Gs.
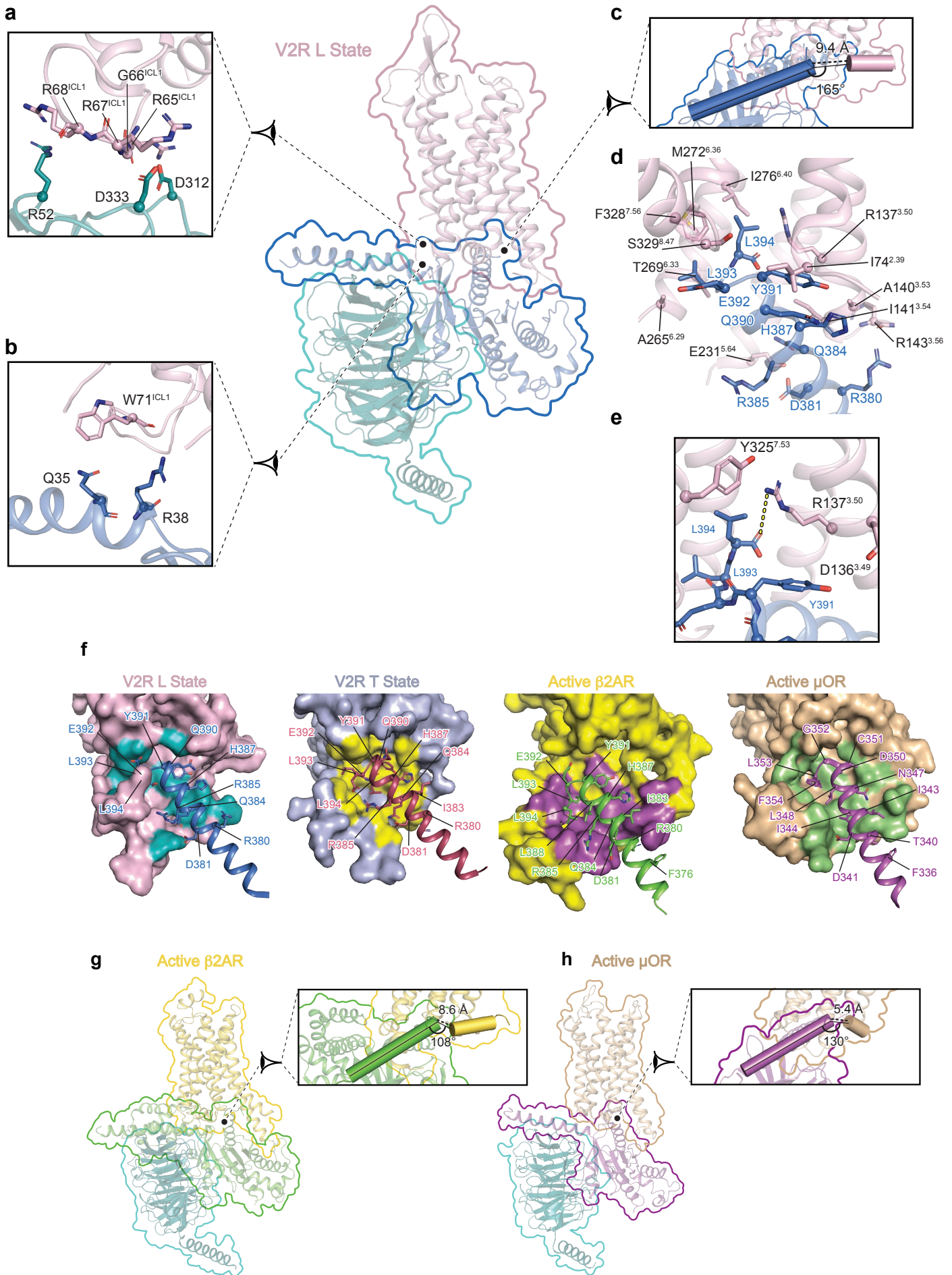
Extended data Figure 7 | Interface of the V2R L state with Gs. Interactions between V2R and Gs heterotrimer are shown. Specific interfaces are depicted, and residues in close proximity (within a maximal 3.9 Å distance) are highlighted (pink for V2R, turquoise for Gβ subunit, blue for Gα subunit). **a**) Interaction of V2R icl1 with Gβ subunit. **b**) Interaction of V2R icl1 with N-terminal helix of Gα subunit. **c**) Positioning of C-terminal h5 helix of Gα subunit relative to V2R helix 8. The distance between Gα and helix 8 is indicated. Angle between these two domains is shown. **d**) Interacting residues between the C-terminal h5 helix of Gα subunit and V2R. **e**) Zoom on an ionic bridge between the C-terminal free carboxylic moiety of h5 helix of Gα subunit and V2R R137[3.50]. **f**) Comparison of class A GPCR-Gα protein interfaces. The V2R-Gαs interfaces of L and T states are compared to those of the β2AR-Gαs and μOR-Gαi complexes. The h5 helix of the Gα subunit is shown for each complex with its residues indicated. The residues of receptors in contact with the Gα C-terminal are coloured. **g**) and **h**) Position of the C-terminal h5 helix of Gα subunit relative to receptor helix 8 in active β2AR-Gs and μOR-Gi complexes, respectively. Distances and angles between these domains are indicated as in panel c.

Extended Data Movie 1 | Representation of the flexibility of the signalling complex. This animation represents the first four eigenvectors computed by multi-body refinement analysis, which explain 78% of the variability of the cryo-EM projections (see Extended Data Fig.4).

Extended Data Movie 2 | PCA analysis obtained from molecular dynamics simulations. This animation shows the motion described by the first 3 eigenvectors from a PCA analysis starting from the L model. The PCA was performed on protein Cα atoms using MD trajectories representing about 2.6 µs of aggregated simulation time (see Supplementary Fig. 9).

Extended data Table 1: Cryo-EM data collection, refinement and validation statistics

	AVP-V2R-Gαsβ1γ2-Nb35 (L state) (EMD-12128) (PDB 7BB6)	AVP-V2R-Gαsβ1γ2-Nb35 (T state) (EMD-12129) (PDB 7BB7)
Data collection and processing		
Magnification	165,000	165,000
Voltage (kV)	300	300
Electron exposure ($e^-/Å^2$)	50.19*/41.19**	50.19*/41.19**
Defocus range (µm)	-0.8 to -2.2	-0.8 to -2.2
Pixel size (Å)	0.81	0.81
Symmetry imposed	C1	C1
Initial particle images (no.)	3 566 007	3 566 007
Final particle images (no.)	147,524	420,953
Map resolution (Å)	4.2	4.4
FSC threshold	0.143	0.143
Map resolution range (Å)	3.2-5.6	3.8-6
Refinement		
Model resolution (Å)	4.0	4.3
FSC threshold	0.5	0.5
Model resolution range (Å)	3.2-5.6	3.8-6
Map Improved resolution (Å) (cryoresolve)	4.0	4.1
Map sharpening B factor ($Å^2$)	-141.6	-75
Model composition		
Non-hydrogen atoms	7955	8040
Protein residues	1017	1022
Ligands	0	0
B factors ($Å^2$)		
Protein	87.61	72.14
Ligand	163.31	106.00
R.m.s. deviations		
Bond lengths (Å)	0.007	0.007
Bond angles (°)	0.947	1.027
Validation		
MolProbity score	2.55	2.81
Clashscore	28.39	37.36
Poor rotamers (%)	0	0
Ramachandran plot		
Favored (%)	87.46	78.74
Allowed (%)	12.54	21.26
Disallowed (%)	0	0

*Dataset 1, **Dataset 2